Slow Light Mach-Zehnder Interferometer for Optical Label-free Biosensing

By

Kun Qin

Thesis

Submitted to the Faculty of the

Graduate School of Vanderbilt University

in partial fulfillment of the requirements

for the degree of

MASTER OF SCIENCE

in

Electrical Engineering

May, 2014

Nashville, Tennessee

Approved:

Sharon M. Weiss, Ph.D.

Yaqiong Xu, Ph.D.

Acknowledgements

This work would not have been possible without the support of the National Science Foundation funding. I am grateful to my Thesis Committee who has provided me extensive guidance and taught me a great deal about both scientific research and life in general. I would especially like to thank Dr. Sharon Weiss, the chair of my committee. As my instructor and advisor, she has taught me patiently throughout my life during the Master program study. She has shown me what a good scientist should be by her own example.

I appreciate those who I have had the pleasure to work with during this and other related projects. I am especially indebted to Mr. Shuren Hu, my senior lab-mate and partner, who has helped me and guided me during the research process and quotidian life.

Nobody has excelled the importance in the pursuit of this project over the members of my family. I would like to thank my parents, who have supported most of the financial expense during my study in the United States. They showed me love and guidance in whatever I pursue. Finally, I wish to thank my loving and supportive girlfriend, who provides unending inspiration.

Table of Contents

List of Tables

List of Figures

Chapter 1: Introduction

Biotechnologies have attracted increasing attention during the past two decades due to their capability for improving our living standard through, for example, point-of-care diagnostic devices and devices for supporting our homeland security. One major subset of these technologies is biosensors, which have thrived due to new findings across the fields of material science, optics and electronics. According to a recent report, the value of the market for biosensing is very promising: the global market for biosensors is estimated to reach $16.8 billion by 2018 [1].

A biosensor is defined as an analytical device that is capable of transducing biomolecule binding events into mechanical, thermal, electrical or optical signals. According to the signal type that is transduced, a biosensor can be categorized as one of four types: mechanical, thermal, electrical, or optical biosensors. Among these possible methods of biosensing, optical biosensors excel due to their high sensitivity and reliability, large potential for chip-scale integration, and versatile sensing platform including the capability of trapping and manipulating at the scale of nanometers.

The sensing performance of an optical biosensor can be characterized by its absorbance, transmission, fluorescence intensity, polarization, or reflectivity. While many optical sensors are label-free and do not require significant sample processing before measurement, fluorescence intensity-based optical biosensors require molecular labeling with fluorescent tags, which necessitates additional resources of labor force, time and expensive laboratory equipment. Furthermore, the labeling processes may also interfere with the function of a biomolecule, leading to improper sensor performance. Accordingly, this work focuses on a sensitive and label-

free method of detecting molecules, which is compatible with the detection of viruses, DNA, proteins, and antibodies, and is particularly promising for implementation in next-generation clinical diagnostic assays.

Most label-free optical biosensing technologies are refractive index based, which can be further categorized as surface plasma resonance, interference, or photonic cavity according to their function mechanism. These types of biosensing technology mostly rely on measuring a refractive index change in the near vicinity of the device. The refractive index change could be due to a change in analyte concentration change or the presence of molecules. For most photonic devices, optical modes are primarily confined within the device with an evanescent tail that can extend hundreds of nanometers away from the surface of the device. These optical modes determine the output spectrum of the device, which may be either a resonant spectrum or interference fringe. A refractive index change in the vicinity of the optical device will change the effective refractive index of the optical modes, leading to a red-shift in the output spectrum when the effective refractive index increased. The magnitude of this shift as a function of the surrounding bulk refractive index change is figure of merit representing the sensitivity of the biosensor device.

1.1 Fundamentals of Optical Biosensing

By solving Maxwell's equations and applying first order perturbation theory, we have [2]:

$$\nabla \times \nabla \times |E\rangle = (\frac{\omega}{c})^2 \varepsilon |E\rangle \quad (1)$$

Once assume the change of the permittivity of the dielectric media caused by the attachment of the biomolecules to be Δε, and the perturbed electric field distribution is $|E^{(0)}\rangle + |E^{(1)}\rangle$, where $|E^{(0)}\rangle$ is the original electric field which is related to the energy density with in the sensing area (typically a cavity or slow light region). $|E^{(1)}\rangle$ is the first order approximation, and corresponds to the spectrum shift by $\omega^{(1)}$. Here, for the convenience of expression, we select $\omega^{(0)}$ as the frequency to represent the initial spectrum. Then we may rewrite the first order perturbation correction as [2]:

$$\omega^{(1)} = -\frac{\omega^{(0)}}{2}\frac{\left\langle E^{(0)}\middle|\Delta\varepsilon\middle|E^{(0)}\right\rangle}{\left\langle E^{(0)}\middle|\varepsilon\middle|E^{(0)}\right\rangle} \tag{2}$$

where $\langle E^{(0)}|\Delta\varepsilon|E^{(0)}\rangle$ is the perturbed electric field energy and $\langle E^{(0)}|\varepsilon|E^{(0)}\rangle$ is the entire electric field energy. Thus the bio-molecular attachment can be reflected into the shift of transmission spectrum or variation of light intensity directly. This also defined the sensitivity for target bio-molecular detection. Therefore, in order to comprehend the factors that may influence the detection sensitivity better, the equation can be rewritten as:

$$\omega^{(1)} = -\frac{\omega^{(0)}}{2U_{total}}\int E^{(0)*}\Delta\varepsilon E^{(0)}dV \tag{3}$$

where U_{total} is the total electric-field energy within the sensing area before the molecular attachment, and $\langle E^{(0)}|\Delta\varepsilon|E^{(0)}\rangle$ is rewritten in a form of integration within the corresponding region to express the spatial overlap between the modal electric filed and the sensing area. This equation clarifies the relationship between the spectrum shift, which is the indicator of evaluating the molecular attachment, and three arguments, which are $E^{(0)}$, $\Delta\varepsilon$ and dV, respectively. These

are also the key points for researchers from all over the world to work on different topologies to balancing, engineering and manipulating the three parameters above to achieve the best performance for the purpose of biosensing without sacrificing the compactness of the device.

1.2 Photonic Label-free Biosensors

Nanophotonic sensors mainly can be divided into two categories: plasmonics based sensors, such as surface plasmonic resonance (SPR) sensors [3], and silicon photonics sensors, such as Mach-Zehnder interferometer (MZI) [4-11], Bragg grating based Fabry-Perot cavity [12-14], photonic crystal cavity [15-21], micro-disk resonator [22-24] and micro-ring resonator [25-30].

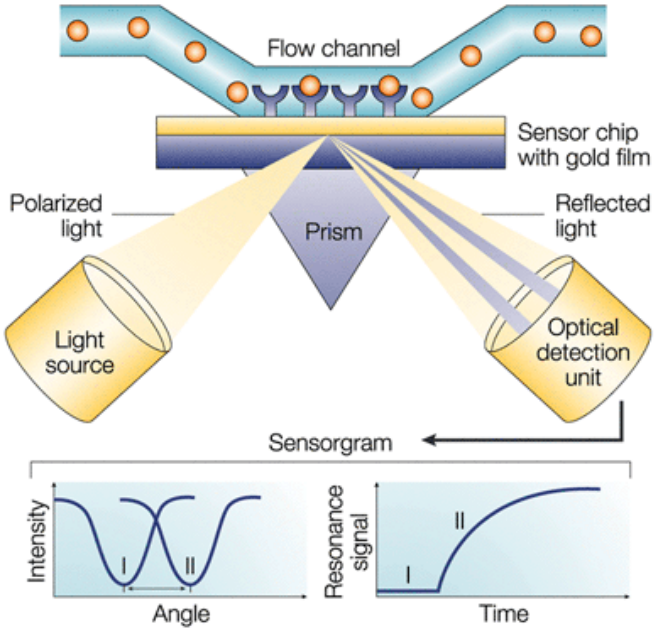

Fig. 1 Commercialized optical biosensor based on surface plasma resonance (SPR) (Figure from Ref. [3])

SPR sensors have been successfully commercialized and widely used in biological/ medical research as well as clinical test. The schematic illustration is shown in Fig. 1. Incident light is shown from a laser resource on the left. Refractive index changes in the vicinity of the surface of

the sensor are detected. Depending on the mass variation at the surface, the angle of sharp shadow induced by SPR in reflected beam will correspondingly shift. Thus the molecular binding process can be characterized by measuring the angle that shadow shifted. This angle shift can be non-invasively recorded for kinetic analysis of the relationship between resonance angle and time. Although this method has been verified as a mature commercialized high sensitivity label-free biosensor, it requires bulky and expensive equipment to carry out measurement, and hard to achieve high through-put, multiplexing detection.

Silicon photonic biosensors have small footprint and high sensitivity, which make them superior platform for ultrasensitive, high throughput multiplexing sensing. Moreover, silicon micro-ring resonators are CMOS compatible. These features make silicon photonic devices easy for on-chip integration interfacing with both electrical components and microfluidics add-ons.

Micro-ring resonator, as an example of silicon photonic sensors, has been commercialized by a start-up company and sensors based on this technology are available on the market now.

Fabry-Perot cavity devices often either require multiple fabrication steps (multi-layer devices [14]) or high precision fabrication, which remains challenging for massive production in the near future. Micro-disk resonator is based on whispering gallery modes (WGM), which supports multiple modes. The corresponding detection performance degeneration resulting from crosstalk between modes is one of the drawbacks for this type of device. Although micro-ring resonators have the advantage of supporting single mode transmission and easy fabrication, as well as multiple cycling within the ring-region that will prolong the interaction length between light and target molecules, the tradeoffs between micro-rings' confinement for the light and detection range due to periodic transmission spectrum is a bottleneck that still needs improvement. While

micro-rings with smaller radii have larger spacing between transmission peaks, the larger the radius of the ring is, the less bending loss there will be. Hence, larger rings have enhanced mode confinement inside the rings, which is reflected by quality factor (Q factor), a parameter denoting photon lifetime inside a cavity. However, enhancement of the Q-factor will sacrifice the footprint of a device. Selection of TE or TM mode is another issue concerning micro-rings. For most integrated devices, TE mode light is easier to excite and more widely used while TM mode light will have greater overlap with target molecules on the surface.

Unlike resonance-based optical biosensors, MZI sensors utilize interference to detect small refractive index perturbations. Their capability of phase and intensity modulation as well as broadband operation enable their application in silicon modulators by industries [30]. In addition, single mode MZI is easy to fabricate, which is another reason that they are prevalent. Furthermore, the non-resonant character makes the operation wavelength less restricted by the facility for various research groups, which will accelerate the research progress. Finally, MZI devices are more immune from thermal fluctuation that degenerate the range of detection compared to high Q factor resonator devices [31]. Hence the MZI is a popular research area of optical biosensors.

1.2.1 Mach-Zehnder Interferometer

MZI is a classical optical setup to measure small optical length variation according to interference fringe, as illustrated in Fig. 2 [32]. Each MZI setup contains two arms: one is noted as reference arm that will either not change or slightly change during the experiment process, and the other is the experimental arm that will allow test material to interact within the region where light is propagating thus to change the total optical length on this experimental arm. The light in

these two arms will combine after a certain length of propagation; the output signal will demonstrate a fringe pattern due to interference effect, shown as in Fig. 2 (b) [33]. Once there is any phase change, fringe will correspondingly shift upward or downward. Due to the fringe is a pattern that contains the information amplified by the distance between junction of beam combination and detection screen, a minor change inside the experimental arm will result in a relatively large fringe shift. Thus a traditional MZI can be used for gas sensing or thin film index characterization on behalf of its high sensitivity characteristics.

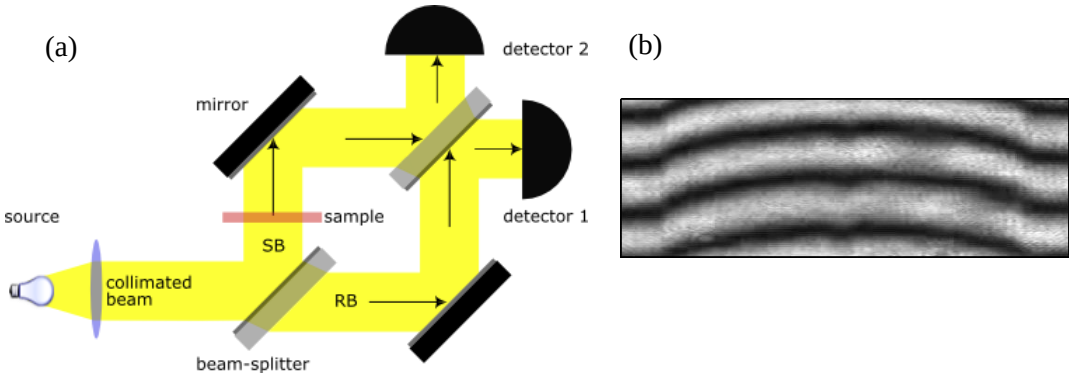

Fig. 2 (a) Traditional optical free space MZI setup (Figure from Ref. [32]); (b) Interference fringe of MZI (Figure from Ref. [33])

Currently, with the booming of CMOS technology, many researchers turn to integrate MZI on to the micro/nano platforms. Fig. 3 shows an example of an MZI fabricated on a silicon-on-insulator (SOI) wafer that was fabricated as part of this thesis work. By inheriting the advantage of high sensitivity and low limit of detection (LOD), various integrated MZIs were extensively used in the field of biosensing, such as silicon nitride waveguide [7-9], SOI [4], porous silicon [6], and tapered optic fiber [10,11]. As the size shrinks down to the scale of micro meters, the measurement of MZI output signal has to be readjusted correspondingly. Instead of observing the entire shift of fringe on the detection screen, most integrated MZI device will detect the output

intensity. By kinetically measuring the output intensity at a fixed wavelength during the sensing reaction process, the intensity will fluctuate sinusoidally due to the interference resulted from phase shift difference between two arms. The total number of fluctuation periods can reflect the phase shift that sensing arm has experienced. This concept is discussed in detail in the following paragraphs.

Fig. 3 SEM image of SOI based MZI

For an integrated MZI, the schematic illustration is shown in Fig. 4. The upper arm is a sensing arm whereas the other corresponds to reference arm. The electric field and light intensity inside the sensing arm is denoted as E_S and I_S. Accordingly, electric field and light intensity within the reference arm is labeled as E_R and I_R. In the figure, only the sensing arm is exposed to ambient environment. Biomolecules, as represented using red blocks and "Y" shaped linkers, are covalently bonded onto the surface of sensing arm. Since the input light is coherent, the phase information contained by electric field at input port for each arm should be the same. Thus, according to Maxwell's equations, electric field inside the sensing arm can be written as $\mu E_I e^{j(\omega t+kz)}$ and that of the reference arm should be $\tau E_I e^{j(\omega t+kz)}$, where E_I is the original input

electric field amplitude, μ^2 and τ^2 denote the ratios of distribution of energy into each arm. Thus, we have $\mu^2 + \tau^2 = 1$. We also have z denotes the current position of the electric field; k_1 and k_2 are propagation constants, as known as wave vectors, which can also be written as $2\pi n_{1,2}/\lambda$, where n is the refractive index, for each arm.

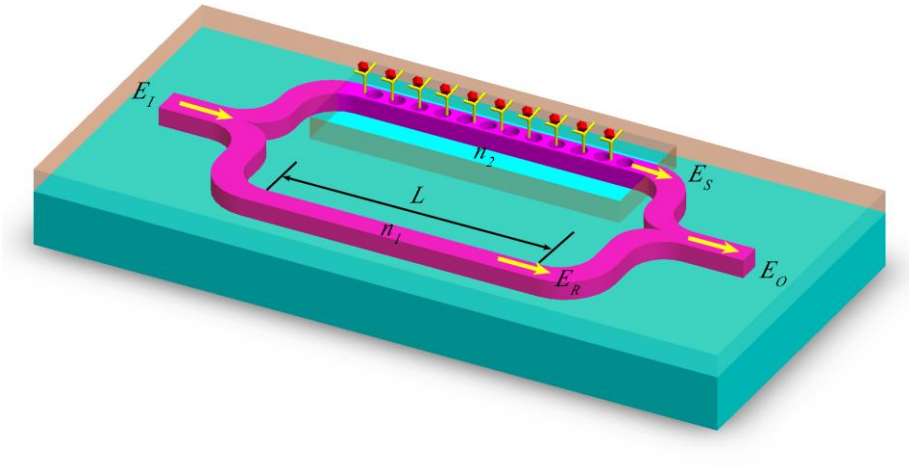

Fig. 4 Schematic illustration of integrated MZI sensor

At the input and output ports, the wave vector should be the same due to the same incident light source and waveguide medium. After propagating through two arms, the electric field for each arm will be expressed in the following equations:

$$\begin{cases} E_S = \mu\alpha E_I e^{j\omega t + jk_1(L+\Delta L)} \\ E_R = \tau\beta E_I e^{j\omega t + jk_2 L} \end{cases} \tag{4}$$

where L and $L+\Delta L$ denote the physical length (length of waveguide in this case) light has experienced in each arm, α and β are damping coefficients induced by either device or waveguide, such as scattering caused by waveguide sidewalls or median damping due to electronic resonance. By rewriting the form of wave vector, the optical path difference can be

expressed as $n_1(L+\Delta L)-n_2L$. Thus the phase shift can be rewritten from the optical path difference above, which is $2\pi[n_1(L+\Delta L)-n_2L]/\lambda$. To express the output electric field by adding up the two components above, it can be written as:

$$\begin{aligned}\overrightarrow{E_O} &= \overrightarrow{E_R} + \overrightarrow{E_S} \\ &= (\mu\alpha e^{2\pi j n_1 (L+\Delta L)/\lambda} + \tau\beta e^{2\pi j n_2 L/\lambda}) \cdot \overrightarrow{E_I} e^{j\omega t}\end{aligned} \tag{5}$$

where $\overrightarrow{E_S}$ and $\overrightarrow{E_R}$ represent the vectors of E-field in each arm, $\overrightarrow{E_I}$ and $\overrightarrow{E_O}$ stand for the vectors of E-field at the input and output port of MZI, Thus the intensity should be:

$$\begin{aligned}I_O &\propto \left|\overrightarrow{E_O}\right|^2 = \left|\overrightarrow{E_R} + \overrightarrow{E_S}\right|^2 \\ &= E_I^2\{[\mu\alpha\cos(\frac{2\pi n_1(\mathrm{L}+\Delta\mathrm{L})}{\lambda}) + \tau\beta\cos(\frac{2\pi n_2\,\mathrm{L}}{\lambda})]^2 + [\mu\alpha\sin(\frac{2\pi n_1(\mathrm{L}+\Delta\mathrm{L})}{\lambda}) + \tau\beta\sin(\frac{2\pi n_2\,\mathrm{L}}{\lambda})]^2 \\ &= E_I^2\mu^2\alpha^2 + E_I^2\tau^2\beta^2 + 2E_I^2\mu\tau\alpha\beta\cos\{\frac{2\pi[\mathrm{n}_1(\mathrm{L}+\Delta\mathrm{L}) - \mathrm{n}_2\mathrm{L}]}{\lambda}\} \\ &= I_s^2 + I_R^2 + 2\sqrt{I_S I_R}\cos(\Delta\varphi)\end{aligned} \tag{6}$$

where $\Delta\varphi = \frac{2\pi n_1(\mathrm{L}+\Delta\mathrm{L}) - n_2\,\mathrm{L}}{\lambda}$, is the phase shift induced from the optical path difference between two MZI arms. Hence in modern technology, people fixed the operation wavelength. By simply detecting the output intensity, we can sense how much phase shift has been experienced by the light and consequently reflects the environmental refractive index change when the physical lengths of the arms of the MZI do not change.

Other than intensity monitoring method, one can also focus on the spectrum shift to detect the index change [11]. By sweeping the spectrum in a certain range continuously, we can have the real-time spectrum shifting curve, which will also reflect how much optical path change has

taken place. This mechanism is especially suitable for the surface sensing, since this method is sensitive for minor changes and will not rely on the mechanical stability of measurement setup.

The sensitivity S of an MZI biosensor is typically defined as the phase change over the environmental index variation on a specific device length, which is also expressed as:

$$S = \frac{\Delta\varphi}{\Delta n \bullet L} \tag{7}$$

where $\Delta\varphi$ denotes the phase change due to the environmental index change, Δn is the environmental index change and L is the length of device region or sensing region. Compared to this definition, traditional optical biosensor has a sensitivity most often defined as the spectrum shift over the environmental index change, which is $S=\Delta\lambda/\Delta n$ and named spectral sensitivity. Thus the unit of this definition is nm/RIU, where RIU stands for refractive index unit. According to the principle of MZI, the output signal is differentiating the optical path between two arms. Therefore with the same treatment to the MZI device, the longer the sensing arm is, the more phase shift will be. This is also the reason that typical size of integrated MZI is 1-15mm. Under this dimension, an MZI sensor can reach ultra-high spectral sensitivity (1100nm/RIU [11] - 7000 nm/RIU [10]), as well as ultra-low LOD (7×10^{-6} RIU [8]). However, increasing the size of a device does not stick to our original intention of this integrated MZI biosensors. Hence, the commonly applied MZI sensitivity can be used to show the potentially sensitivity of a MZI device, as discussed in the next section. It is obvious that by enhancing the size of MZI, the performance is easy to be upgraded to achieve ultra-low LOD due to the definition of $\Delta\varphi$. Nonetheless, large device footprint is not suitable for the chip-scale integration for future improvements.

Other than sensitivity, LOD is also a figure of merit for evaluating the performance of an MZI biosensor. It is defined as the lowest effective index change in the vicinity of the device that can be detected by the sensor. On one hand, this is related to the steepness of the spectrum peak or valley. The steeper the slope is, the easier the shift can be distinguished from the previous spectrum, and vice versa. On the other hand, this is also determined by the minimum change detected that is larger than the noise level of the whole system. The system noise level is defined as the standard deviation of the output signal for a system at the same condition over a certain period of time [9]. Similar to the mechanism of sensitivity: the larger the device is, the larger cumulative phase change results from the same index variation in the vicinity will be. This is the main attraction of MZIs for many researchers.

Recent developments in MZI biosensors

Ever since the first attempt of integrated MZI biosensor 20 years ago [5], researchers all over the world have been dedicated to improving the performance of MZI biosensors. Researchers from Spanish National Research Council implemented this idea on the platform of silicon nitride platform to avoid thermal fluctuation [8], by applying the sensing arm as long as 15mm, the LOD can be enhanced to 7×10^{-6} RIU. Then almost ten years later, researchers from Institute of Microelectronics from Singapore proposed slot waveguide based MZIs on the silicon nitride platform [7,9]. Their 7mm long sensing area combined with the slot waveguide effect provides larger mode overlap which results in the more intensive phase change during the process (Slot waveguide theory is discussed in the next section). This work reported a sensitivity of 15,600 rad/RIU-cm. A group in National Research Council Canada implemented MZI on the platform of SOI [4]. Unlike the previous device, this group fully used the high index contract between silicon

and buried oxide layer. This device was fully etched using reactive plasma etching. Although the total length of the MZI is 2mm but LOD of the device is ~10 fg for the surface sensing experiments. Other than traditional waveguides based MZI, recently a group also demonstrated a MZI biosensor with the usage of porous silicon [6]. Due to the porous structure, much larger surface area is provided. When light propagated inside of the PSi waveguide, much larger mode overlap with surroundings can be predicted. This work has achieved the sensitivity as high as 13,000 rad/RIU-cm. Apart from on-chip type of MZIs, micro MZIs based on fiber optics are also widely used [10,11]. People used tapered fiber whose core size is approximately 2μm as the sensing arm to detect the index variation in the vicinity. This method typically has ultra-high spectral sensitivity [10] (~7000 nm/RIU, which is 19,000 rad/RIU-cm for phase sensitivity) because tapered region has squeezed out large portion of mode distributed at the surface of tapered fiber as evanescent tail, which is the main mechanism for optical sensing theory. However, this method is neither CMOS compatible nor adaptable to the sensing of small amount of biomolecules. Thus this method is less applied in the surface sensing field but more in the bulk sensing field. In summary, although MZI does have high spectral sensitivity as well as low LOD, typical size at the scale of millimeters is preventing this structure from further development.

1.2.2 Slow Light Structure

In order to overcome the drawback of large device footprint, one can either increase the mode overlap with optimizing the topology of MZI (such as slot waveguide as mentioned) or enhance the group index, as known as slow light effect.

Slow light effect is based on either photonic crystal theory or cascaded micro-ring resonators [16,21,34]. However, for the aspect of smaller footprint, we will merely discuss the effect caused by photonic crystal structure. Recalling the definition of crystals, crystal is defined as a series of material consists of atoms or molecules that will result in periodic potential distribution. In the case of lattice arrangement prohibiting the electrons from propagating in three directions, a complete band gap will occur. In analogue to the band gap theory in the discipline of semiconductors concerning electronics, the photonic band gap (PBG) exists in dielectric media whose permittivity periodically varies in the scale of light wavelength (a few hundred nanometers). The sensing arm of device illustrated in Fig.4 shows an example of 1D photonic crystal. This structure will cause destructive interference of certain photonic modes. Photons at the corresponding wavelengths are prohibited from propagating in the directions with existence of PBG.

According to the number of dimensions where light is prohibited from propagating, photonic crystal can be categorized into 3 groups: 1D, 2D and 3D photonic crystal. Despite 3D photonic crystal has made some achievement recently [35-37], the design and fabrication of 3D photonic crystals remain challenging. Thus people typically use 1D or 2D photonic crystal for different applications, such as biosensing [20], lasers [38], or modulation [39].

The simplest model of the 1D photonic crystal is a Bragg Mirror, which is comprised of dielectric media whose refractive index is periodically modulated. This structure will induce the 1D PBG confinement in the direction corresponding to the refractive index modulation. Currently, more and more designs incline to use line type air hole arrays in waveguide to form a 1D photonic crystal [40,41].

In contrast to simple 1D photonic crystal, 2D photonic crystal has light confinement in two different directions which makes the mode volume smaller than 1D photonic crystal when applying the same intensity of confinement. This structure typically consists of 2D arrays of air holes in the medium.

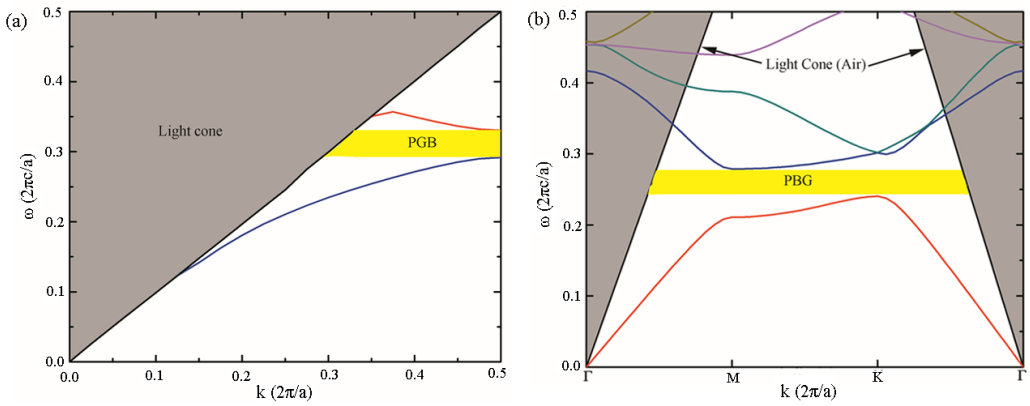

Fig. 5 (a) Band diagram of 1D photonic crystal; (b) Band diagram of 2D photonic crystal

As illustrated in Fig. 5, (a) and (b) are the PBG of 1D and 2D photonic crystal, respectively. This band diagram is calculated using MEEP and MIT Photonic Bandgap (MPB) [42]. Since 1D photonic crystal only confine the light in one direction, the wave number is only plotted in the periodic structure direction. 2D photonic crystal has periodic structure in two dimensions, thus the x-axis of band diagram is plotted along three basic vectors in the first Brillouin zone of photonic crystal lattice. The boundary of grey shaded region is called light cone, whose inverse of the slope defines the refractive index of the background (in the case of Fig. 5, the background is set as air). Each curve within the band diagram represents a mode that can exist in the designed structure, whereas the region where no curve exists (yellow highlighted region) forms a PBG. Consequently, light frequencies located in PBG range will be prohibited from propagating

in corresponding direction. Both 1D photonic crystal and 2D photonic crystal can be deciphered or designed using this method.

Accordingly, when one or multiple defects are introduced into the structure, optical modes can emerge within the PBG. The defects can be, for example, a line defect with missing holes or a line defect that consists of different sizes of holes among the entire array of holes that constitute the photonic crystal structure, forming a cavity. Depending upon the types of defect, defect modes can be either a line or a dot locating in the region of band gap.

To take the 2D photonic crystal band diagram as an example, from the bottom to the top, there are five curves in different colors. Each of them represents different modes that this structure can support. The bottom one (red) is the first order mode. In the case of silicon based photonic crystal, under this mode, light is distributed evenly and confined within the region of silicon. The blue curve stands for mode where light is distributed in the air holes. Note that all modes we discussed here are TE (Transverse-Electric) mode, since standard 2D photonic crystal with silicon base can only open a PBG in this polarization. As the higher orders of the mode approach closer to the light cone, the mode is more likely to leak into the background, which means the device will perform less confinement for light. Thus, we need to bend the band gap further away from the light cone to avoid unnecessary loss.

The definition of group index is the quotient of speed of light in vacuum and speed of wave packet. It is written as the following equation:

$$n_g(\omega) = \frac{c}{v_g} = c \cdot \frac{\partial k}{\partial \omega} = \frac{\partial}{\partial \omega}(\omega \cdot n(\omega)) = n(\omega) + \omega \frac{\partial n}{\partial \omega} \tag{8}$$

In the equation above, $n(\omega)$ is the refractive index at the frequency of ω, k is the wave number inside a waveguide. Thus, according to the axes of band diagram, the inverse of local derivative of each curve represents the value of the $\omega \bullet (\partial n / \partial \omega)$ on the right-hand side of Eq. (8). Knowing that the band diagram will be flat at the junction of wave vector in the Γ→M and M→K directions, the group index will theoretically approach infinity. This flatness phenomenon is intuitively explained as when the light propagates with a wavelength near band edge in the Γ→M direction, the quasi-prohibition in M→K direction will restrict the light from propagating outside the waveguide, which means the vertical component of wave vector can be larger than plain waveguide whereas the propagation number is extremely small. This quasi-prohibition leads to the zero group velocity. Therefore the effect that the device's group index is enhanced to be extremely high is called "slow light effect". With this group index, group velocity, which is v_g in Eq. (8), for this device is very low which lead to the origin of the name of this concept. The corresponding region is called "Slow Light Region", where the light will be "tied" within the region, but not confined. Thus slow light can be treated as a condensed waveguide, which will sequentially decrease the footprint of total device. That is the origin of the theory that slow light can decrease the length of sensing arm.

According to the analysis above, slow light occurs in the photonic crystal structures while the wavelength of propagating light locates approaching the edge of PGB. Thus there are two typical topologies that are capable of applying slow light effect: removing one line of lattice holes to form a line defect [15,16,21] or add lateral trusses to plain waveguide to make the waveguide in the shape of a spine [39]. Both of these two methods confine light within the waveguide region

using PBG. Photonic W1 waveguide has better mode confinement due to stricter PBG condition, whereas trusses based slow light waveguide is easier for fabrication.

Recent developments in Slow Light and Photonic Crystal biosensors

A straightforward way of implementing the photonic crystal or slow light sensing element is to excite the device using broadband white light source and collect data with optical spectrum analyzer (OSA). Several demonstrations have been reported recently to apply these structures for label-free optical biosensing purpose [17,18]. Their structure can either achieve low LOD or high sensitivity.

Furthermore, if a photonic crystal structure contains the hole or layer defect within the arrayed structure, light at a specific wavelength or resonant frequencies will be confined at the defect layer or point along the waveguide direction whereas the total internal reflection will be responsible for the transverse reflection [43]. By detecting the shift of this resonance wavelength is another approach for label-free sensing application. After the significant improvement of nanoscale fabrication, the feature size that a device can achieve ~20nm, which allows us to massively fabricate optimized 1D or 2D photonic crystal with ultra-high precision. These optimized 1D photonic crystals are called nanobeams [40,41]. They have extremely high light-matter interaction (LMI) as well as ultralow LOD which have been treated as one of the most promising topology so far for further diagnostics on behalf of point-of-care [44]. This research group from Harvard University applied a polymeric nanobeam into biosensing and achieved a high spectral sensitivity of 386nm/RIU on a footprint less than $100\mu m^2$.

Fig. 6 demonstrates a few examples of photonic crystal biosensors [15,16,19-21]. The first implementation of the photonic crystal biosensing was reported by M. Lee et al. in 2007 [20],

who have achieved the LOD as low as 2.5fg with a photonic crystal cavity structure. Researcher from University of Texas, Austin enhanced the size of the cavity and engineered the photonic crystal waveguide to optimize the waveguide-microcavity coupling efficiency [15]. This design, for one thing, increased the mode volume to achieve better confinement within the cavity region, thus in turn the mode overlaps with surrounding matter will be improved. Additionally, the better coupling condition leads to higher loaded Q-factor, which made the peak more distinguishable, and thus decreased the LOD. As reported in this publication, the limit of surface sensing detection has been decreased to 0.1 μg/mL converted to 8.8 atto-grams. This is the lowest LOD of this photonic crystal cavity based biosensor.

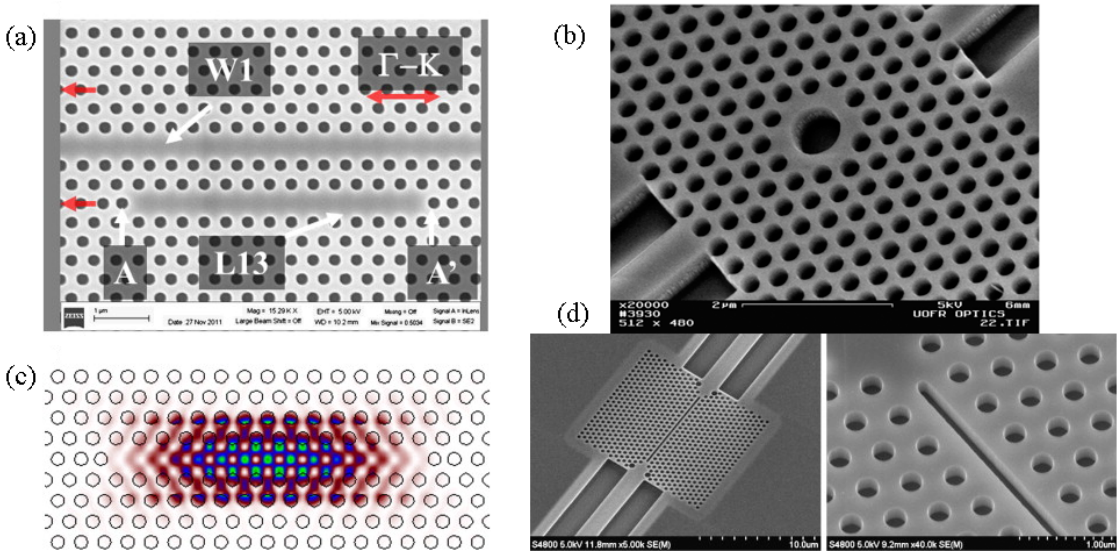

Fig. 6 (a) Slow light based photonic crystal biosensor [15]; (b) Photonic crystal cavity biosensor [20]; (c) Simulated mode distribution of slow light based photonic crystal in (a); (d) Slot photonic crystal waveguide biosensor [21]

Apart from cavity and combined slow light sensing, there is also types of label-free biosensing using pure waveguide based on slow light effect [16]. Due to slow light effect at the band edge of photonic crystal waveguide, apart from group index enhancement, the localized

field intensity will be extremely high. This structure has been applied by researchers from St. Andrews to perform biosensing experiments [21]. Instead of simply applying the photonic crystal waveguide, they integrated a slotted structure into the PhC waveguide. Similar to the slotted waveguide based MZI biosensor, this makes the confined light have even larger LMI. However, the compactness of the device is still one of the most outstanding characters. As from the report, the sensing area was as small as $2.2\,\mu m^2$. A sensitivity of 15nM or $1\,\mu g/mL$ was achieved. Nonetheless, like a teeter-totter, each introduction of minor change inside structure will not only enhance the performance on one aspect but also degrade the character of the device on the other. For this structure, the main drawback is the loss of slotted W1 waveguide. A normal photonic crystal waveguide has the loss of ~30dB/cm, whereas the slotted waveguide will have even higher loss coefficient due to the mode mismatch between the unstructured W1 waveguide and the slotted region. Furthermore, this slotted PhC waveguide device requires undercutting of buried oxide layer. This process will challenge the robustness of devices, which is another main reason why this type of device is not prevalent after several years.

1.2.3 Enhancing Light-Matter-Interaction Using Slot and Multi-Hole Defects Structures

Slot waveguide was firstly proposed by Almeida et al. in 2004 [45]. From Maxwell's equation, the electric field across the boundary of two different dielectric media has the following relation:

$$\varepsilon_1 \overrightarrow{E_1} \cdot \overrightarrow{n_{12}} = \varepsilon_2 \overrightarrow{E_2} \cdot \overrightarrow{n_{12}} \tag{9}$$

Note that $\boldsymbol{E_1}$ and $\boldsymbol{E_2}$ respectively represent the electric field vector located at the surface of medium 1 and medium 2. ε_1 and ε_2 denote the permittivity of each medium and $\boldsymbol{n_{12}}$ is the normal

vector of the surface of two media. When plugging in the values of relative permittivity of air (1) and silicon (11.9) into Eq. (9), we can derive that the electric field in air is 11.9 times higher than that in silicon. By rewriting the equation above, we have:

$$\frac{E_{air}}{E_{Si}} = \frac{\varepsilon_{Si}}{\varepsilon_{air}} \tag{10}$$

Due to this field enhancement induced by the dielectric discontinuity, the electric field can be confined within a very small slot region with high field intensity when two identical waveguides are placed close to each other. In this way, light with strong intensity in the air space in between those two waveguides is guided in the slot (Fig. 7 (e)). Within the slot region, light will have a good mode overlap with the material inside the slot. This will enhance two parameters concerning biosensing, which are the E-field intensity ($E^{(0)}$) and the interaction volume (dV) as well as permittivity change, as we discussed in the first section, but as mentioned before, the lossy mode distribution is a major drawback for this structure.

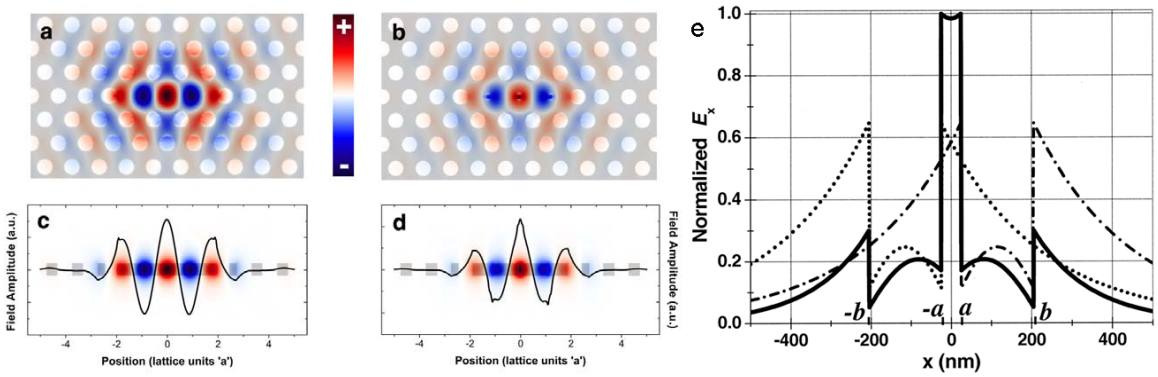

Fig. 7 (a) and (c) Traditional Photonic Crystal Cavity and its mode distribution [46]; (b) and (d) Multi-Hole Defect Photonic Crystal Cavity and its mode distribution; (e) Illustration of field enhancement in slotted structure [45]

To be specific, the high bio-sensitivity of slotted waveguide results from the field discontinuity at the surface of the sidewall of the slot. However, the fabrication process concerning this surface achieved by RIE will make the surface roughness hard to control. This effect will make the slotted waveguide even more lossy. This is also the reason why many researchers incline not to utilize this structure for practical application.

Compared to introducing the line defect, a slot, into the waveguide, Multi-Hole Defects (MHD) will have less influence on the mode profile. MHD-based photonic crystal structures introduce some holes with ultra-small radii (~30-70nm) as defects into a photonic crystal cavity. Kang et al., proposed, studied and applied this structure into biosensing [19,46], as shown in Fig. 7 (a)-(d), where the results showed that the resonant frequency will not be affected very much due to the introduction of MHD. Contrarily, the quality factor will be enhanced since the MHD will intensify the modulation of field within cavity. The mechanism concerning this type of defect is similar to that of a slot waveguide. The only difference is the dimension has been decreased from a line to a small hole. According to their reports, 80% sensitivity increase is observed, which indicates the importance of MHD structure.

1.3 Microfluidics

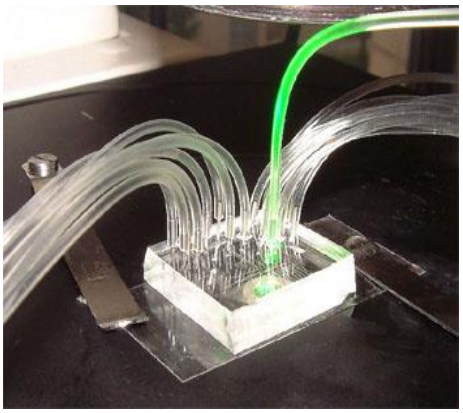

Fig. 8 Demonstration picture of microfluidic system from Computer Science and Artificial Intelligence Laboratory in Massachusetts Institute of Technology (Figure from Ref. [47])

As mentioned at the beginning of this thesis, in order to achieve chip-scale integration for label-free optical biosensors, it is crucial to assemble micrometer scale fluidic channels and transducers together. This leads to the emerging of microfluidics. Microfluidics describe systems that can manipulate small (10^{-9} to 10^{-18} liters) volume of fluids, using channels in the scale of approximately 100 micrometers, as illustrated in Fig. 8. Its characteristics of small footprints, low cost and high sensitivity due to small amount of required samples have been applied to multiple fields, such as biosensing [24,48-55], cell manipulation [56-59] and even device fabrication [60,61].

The corresponding microfluidics fabrication protocol and optimization process will be elaborated in Section 3.2.

Chapter 2: Design and Simulations

2.1 Design of Slow Light MZIs

As mentioned above, slow light can be is a type of medium with ultra-high group index. It has already been demonstrated that slow light MZI can be applied to optical modulation to lower the energy consumption [39]. However, as mentioned before, this structure based on adding lateral trusses to excite slow light effect. Modulating the waveguide using lateral trusses to induce slow light effect will not enhance the LMI since the field was well confined inside the waveguide region. Hence in this work, we approached the slow light effect with nanobeam, aiming at applying the holey structure to enhance LMI. The following section will discuss about the study of design and simulation this novel MZI. All the calculation concerning band diagram were conducted in either MEEP or MPB, all the other Finite-difference time-domain simulation study are carried out with Lumerical FDTD Solutions and Mode Solutions.

Since the type of silicon-on-insulator (SOI) we use has the silicon layer thickness of 220nm, in order to implement single mode waveguide to prevent transmission from crosstalk induced by multi-mode existence, we limited the width of the waveguide to be ~520nm. Given the cutoff width of single mode structure with the thickness of 220nm is 575nm according to mode solving, the fundamental mode will be the only one that exists inside the waveguide.

3D simulation usually cost lots of computation resource. For example, for a 5μm by 5μm simulation region with 1nm size grids it takes an eight-core server about 8 hours to complete the calculation. Therefore, most of the simulations in this section are conducted under the 2D simulation environment. It is noted here that 2D simulation serves as an approximation to the real model. However, it provides guideline for predicting the trend of structure's character.

Usually the 2D and 3D simulation give similar results; minor fluctuation may result from the meshing size variation or slab waveguide approximation. By applying the slab waveguide theory, which is applied for calculating the effective refractive index for multi-layer slab waveguide structure, when assuming the refractive index of silicon is 3.476 and that of silicon dioxide is 1.45, the effective refractive index of a 220nm silicon slab layer on silicon dioxide is 2.83. Therefore during the simulation process, all property of index property of the devices inside simulation model is set to be 2.83 to perform 2D simulations.

For the first step, we used MEEP to solve the band diagram of nanobeam structure. For practical consideration, an operation wavelength needs to be determined around 1550nm. Since all the dimensions concerning scales inside MEEP is normalized to the lattice constant a, so we can fix the width of the waveguide but tune the radius of the holes and lattice constant to make the band edge locate within the range of 1550nm. Within the model we applied for calculation, a computation area of 1 by 12 is applied (with the unit of a). For vertical boundaries, the periodic boundary condition (PBC) is applied to repeat the same structure in horizontal direction. Whereas for vertical direction, a distance of 6 was utilized to isolate the device on both sides, and the boundary condition for these two horizontal boundaries was set to be perfect matching layer (PML) with the thickness of 1. However, in order to keep the feature size of the device remains achievable for fabrication, the feature size is designed larger than 100nm. Therefore, we pick the radii of the lattice holes 130nm and the period to be 360nm. Figure 11 (a) shows the illustration of the model applied for calculation. It is the profile of permittivity distribution generated in MEEP, where the dark part stands for the device, which is silicon in our case, and the bright part is air.

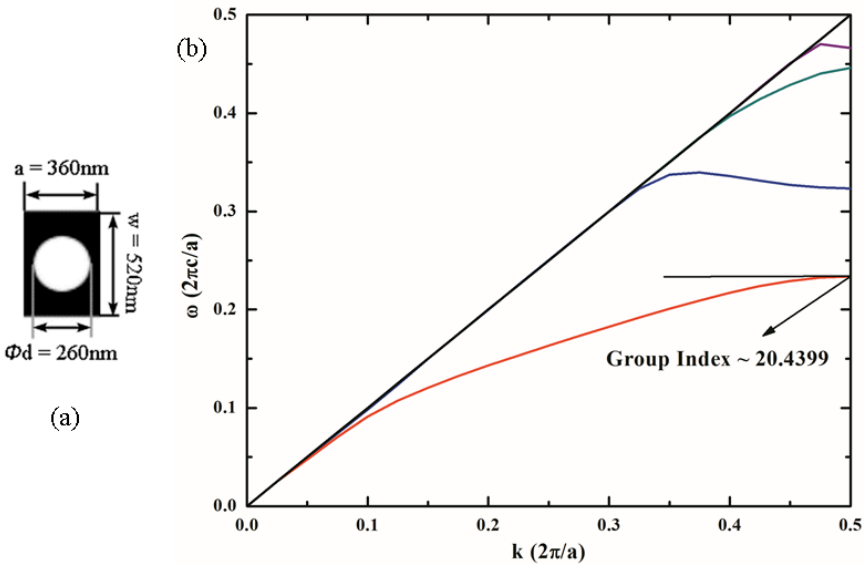

Fig. 9 (a) Unit cell of designed nanobeam for slow light effect; (b) Band diagram of designed nanobeam

The corresponding band diagram is demonstrated in Fig. 9 (b). As mentioned above, the red curve in band diagram stands for the fundamental silicon mode which has the electric field distributed within the silicon, which makes the waveguide less lossy when compared to higher ordered modes. The blue curve is air mode, which corresponds to the mode distributed mostly in the air holes instead of silicon. Air mode is usually good for sensing, because it has large mode overlap with environments. However, it is lossy compare to silicon mode. So we selected the silicon mode for designing. By measuring the inverse of slope of corresponding mode diagram at band edge, we can obtain the group index at the frequency of 0.23(2πc/a) (corresponding to 1565nm in wavelength) to be 20.44, which is 10 times larger than normal silicon waveguide.

However simply calculating the band diagram using MEEP does not demonstrate the transmission performance of the device. Thus we created an identical model and calculated its transmission spectrum using FDTD simulation. This FDTD simulation is performed by Lumerical FDTD Solutions and completed in 2D as well. The model consists of 45 periods of

holes, which makes the total length of the device region to be 16 μm. FDTD simulation region for this model is a 21 μm by 4 μm rectangle with a 500 nm thick PML on horizontal boundaries and 250nm on the vertical boundaries. The meshing size is set to be very small, of which the minimum meshing step is 0.25nm. This is more important to the cases of curved structures, such as round holes, to eliminate scattering issue caused by jigsaw structure boundary. Incident light resource positioned close to the left end of the waveguide, 1.5 μm away from the left boundary of the simulation region, and input from the center of the core waveguide. It is configured to be a Gaussian pulse with the wavelength ranging from 1400 nm to 1700 nm, which guarantees the center wavelength to be 1550 nm. The mode profile is calculated using software integrated mode solution. A TE mode is selected for the consideration of opening a PBG (as mentioned above). The simulation time is set to be 10000 fs, however it is also set to be automatically shut off when the output light intensity is only 10^{-5} of the incident light. A line monitor is placed at the right end of waveguide to collect real-time output signal. The real-time domain data is converted into frequency domain using Fast Fourier Transformation (FTT). The simulated transmission as well as model is demonstrated in Fig. 10. As seen from the curve, the operation wavelength (band edge wavelength) is tuned to locate around 1550nm.

From the transmission spectrum, multiple peaks can be observed. The occurrence of these peaks is due to Fabry-Perot resonance. It is a phenomenon that exists in between a cavity formed with two face-to-face mirrors. Specific wavelengths will make the wave distribution satisfies the standing wave condition (phase matching after propagating a certain distance) which is reflected as different intensity on a spectrum.

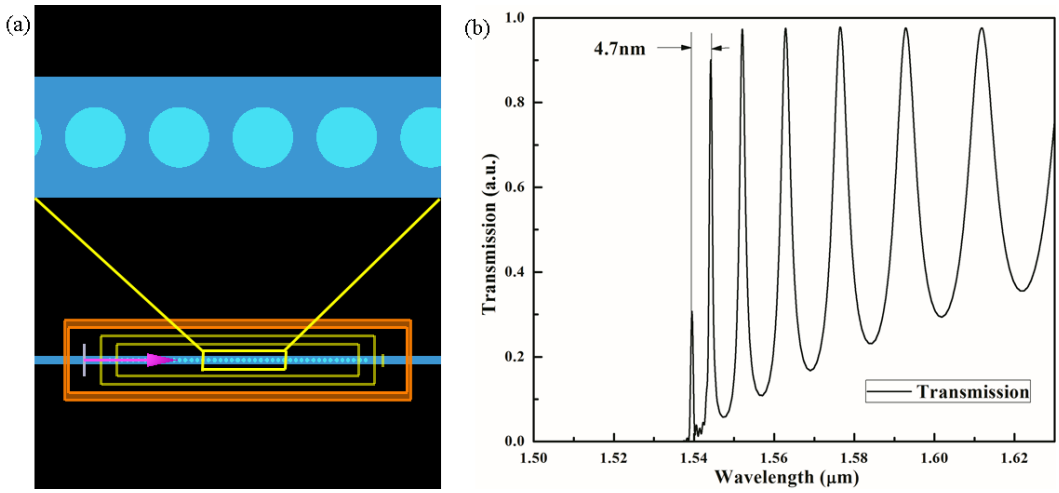

Fig. 10 (a) Illustration of model in FDTD environment; (b) Simulated transmission spectrum of designed nanobeam

Now we introduce the method of evaluating group index from the transmission fringe. In the scenario of a classic Fabry-Perot cavity, the distance refers to the length of light propagating a round trip in the cavity. By evaluating the output spectrum, we can tell the effective cavity length is varying from the band edge wavelength to longer wavelengths. In the case of slow light, the "mirrors" are come from the index contrast between slow light region and plain waveguide region. Defined as the Fabry-Perot resonant condition:

$$2n_g L = m\lambda \tag{11}$$

where n_g denotes the group index at the specific wavelength, which is λ in current case, L is the physical length of the slow light region, m is a positive integer that represents the satisfaction of phase matching condition after one round trip inside the cavity. Thus each peak in Fig. 10 (b) represents a wavelength that satisfies the phase matching condition. Fig. 11 is plotted to illustrate group indices by extracting each peak wavelength from Fig. 10. The highest group index is calculated to be 15.8. Compared to similar case of slow light MZI in [39], who reported 22

experimentally, our design is reasonably lower. However, in order to set aside enough fabrication tolerance, we decided not to further optimize this design. By noting the band gap using blue region, we can tell the trend of group index is increasing and approach to infinity when the wavelength is within the range of band edge. When the wavelength increases far away from the band edge, the group index decreases to the effective index of silicon, which is 2.83 in this case. Since this is derived from Fabry-Perot resonance fringe, the actual band edge is possible to be approached even closer if optimizing the length of slow region or structure. This will make the phase matching condition satisfied occurs exactly at the band edge wavelength. However, for the concern of fabrication, we need to reserve enough fabrication tolerance budget because small deviations in desired device dimensions may cause large changes in transmission profile near band edge because of the sharp group index curve at the proximity of band edge wavelength.

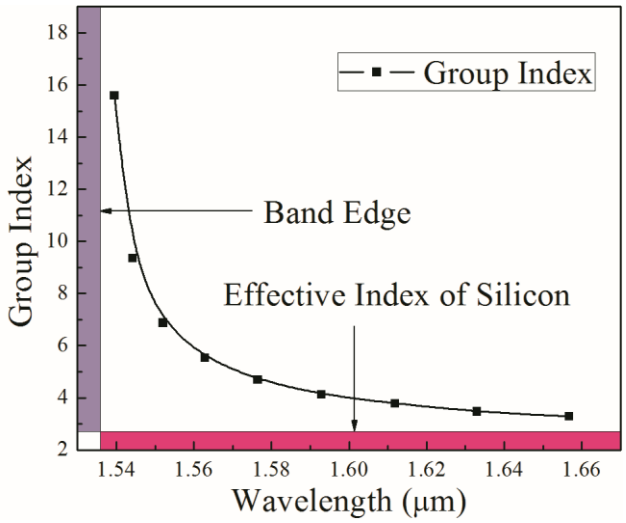

Fig. 11 Group Index contour of designed round hole nanobeam

The way of assuring guided mode is the silicon mode rather than air mode is to evaluate the slow light fringe condensing effect occurs at the shorter wavelength side of the guided spectrum instead of longer wavelength side, since this can tell us which band diagram correspond to the

wavelength we are observing. The reason of this method is the silicon mode will support the frequencies lower than the band edge frequency. Thus from Fig.11, we can tell the silicon mode is confirmed. In consideration of further use, we plotted the electric field distribution overlapped with the index information in Fig.12 to better illustrate it. Within the figure, the black lines are generated from Lumerical software representing the contour of index change, which also stand for the boundary of different dielectric media within the model. Since the round hole stand for the air hole, we can tell from the figure that most of the electric field exist inside the silicon region.

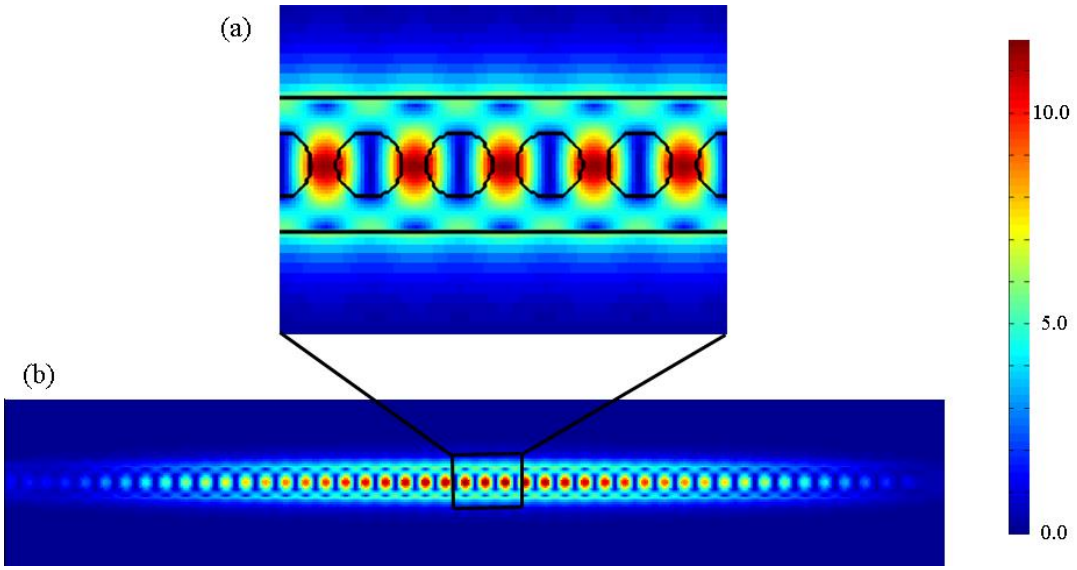

Fig. 12 (a)-(b) Electric Field distribution of designed nanobeam and zoomed in image distribution with the contour of index profile

Next, we investigated the spectrum shifting resulted from the environmental index variation. For this model, we set the index of background medium as well as that of holes to be 1.001. Although the change reflected in the shift of spectrum is small, the trend of this shift reflects the bulk sensing performance.

After calculation, the shifted spectrum was overlapped with the original spectrum and sketched in Fig. 13. The inset is the zoomed in curve for the first peak. From the inset, we can tell the shift of this type of slow light nanobeam is about 0.14nm. Thus the traditional sensitivity is calculated to be 140nm/RIU, which is comparable to those photonic crystal cavity biosensors [15,20]. However, this is a nanobeam biosensor only, which will consume much less time for fabrication compared to the complicated 2D photonic crystal resonator. Since the device is integrated in the waveguide, the total foot print of this device is much smaller than other areal shaped devices.

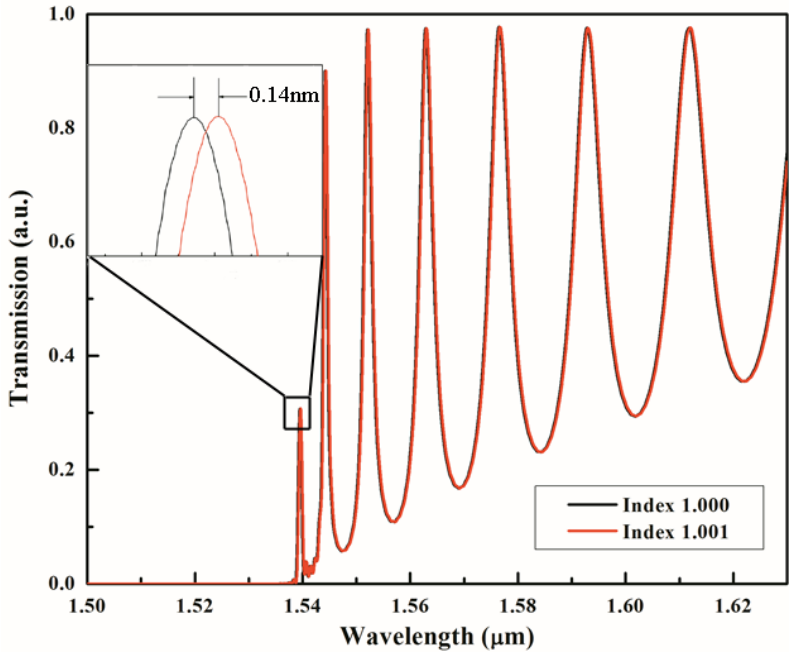

Fig. 13 Spectrum shift of nanobeam due to 0.001 background index change

According to the statement of "slow light can decrease the length of sensing arm", it should have been predicted that the closer to the band edge a wavelength is, the higher sensitivity it will be, since this wavelength range will lead to higher group index which results in higher field intensity enhancement. In this way, larger and larger shift should be observed, from the aspect of

spectrum, as the wavelength increases further from the band edge wavelength. We extracted the shift information from each peak inside Fig. 13 and plotted in Fig. 14 with the black curve. However, the prediction was not verified from the spectrum shifting as illustrated in the black curve of Fig. 14. Contrarily, the first peak is actually the least shifted according to the black curve. This is because the spectral shift actually does not reflect slow light effect which is demonstrated with phase shift. From the fringe, we can see that the slow light effect is reflected in the distance between two adjacent peaks, which means that this needs to be combined into sensitivity.

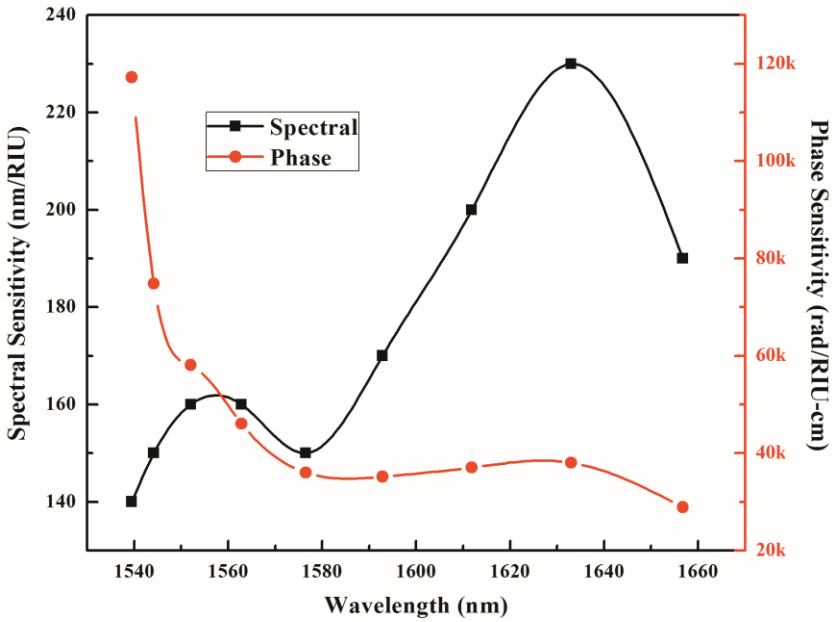

Fig. 14 Spectral sensitivity (black) and phase sensitivity (red) for designed nanbeam at different wavelengths

In order to extract the phase information, we need to convert this spectral sensitivity into phase sensitivity. According to phase matching condition of Fabry-Perot cavity, we know that all peaks represent a phase matching point, meaning that the output phases for these wavelengths are the same as input phases. Thus we know that the shift by one peak-to-peak distance, the

cumulative phase change is 2π, which is actually the same as counting fluctuation periods. Therefore spectral sensitivity can be converted to phase sensitivity (S_{phase}) by using:

$$S_{phase} = \frac{S_{spectral}}{\Delta\lambda \bullet L} \bullet 2\pi \tag{12}$$

where S_l represents the spectral sensitivity at a specific wavelength, $\Delta\lambda$ is spectrum shift needed for 2π phase change and L is the length of slow light region. To take the spectrum of Fig. 13 as an example, by measuring the two peaks that are closest to the band edge, we can tell the for a phase shift of 2π, the spectrum shift should be 4.7nm. Thus by using Eq. 12 above, we can have the phase sensitivity for our device as high as 117,000rad/RIU-cm. In the same way, we can convert all the spectral sensitivity into phase sensitivity, as illustrated in the red curve in Fig. 14.

By using Eq. 12 to calculate the phase sensitivity at each peak in the spectrum, we have the red curve as plotted in Fig. 14. We can observe the phase sensitivity decreases with the decrease of group index when the wavelength increases, which fits our prediction for "higher group index can enhance sensitivity when the device length is fixed". Whereas for the spectral sensitivity, we attribute the general increasing trend of sensitivity to the index degeneration caused by decreased index contrast. When the wavelength increases to even longer, the slow light effect will alleviate, which leads to a decrease in index degeneration. In turn, the spectral shift will decrease. We predict that this spectral shift trend will return to constancy as wavelength increases to even longer. Thus for the rest of discussion and analysis, only the sensitivity (both the spectral and phase sensitivities) at the band edge wavelength is used for comparison.

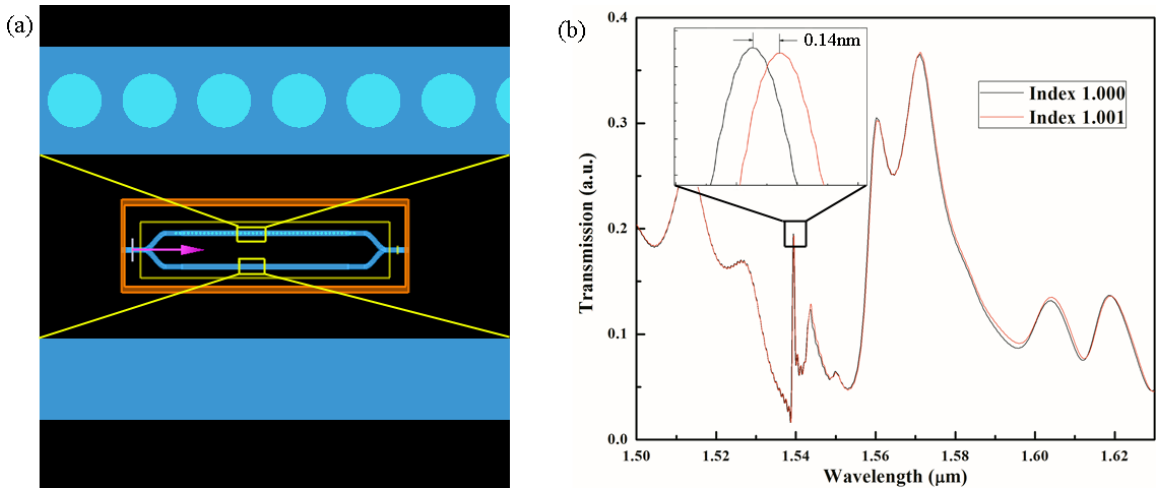

Fig. 15 (a) Single armed MZI model in FDTD environment; (b) Transmission spectrum and shifted spectrum of single armed MZI devices

Next we investigated the scenario of integrating the nanobeam component into the MZI. For the first trial, we only integrate one arm with the nanobeam to demonstrate the sensitivity and compare it to the reported MZI devices. In this round of simulation, the MZI was also implemented using the effective index of silicon. The spacing between two MZI arms is set to be 3μm to isolate each other from unnecessary coupling. Whereas the bending radii of two arms are set to be no smaller than 5μm to avoid bend loss. However, this is the ideal case which only occurs in simulated studies. For practical situation, we may need to balance the radii to avoid scattering caused by defects on the sidewalls which need the radii larger and stitching errors resulted from the fabrication process which requires the footprint smaller. The schematic illustration for simulation is plotted in Fig. 15 (a) and the transmission spectrum is shown in Fig. 15 (b). This transmission looks hard to evaluate because the MZI spectrum has a superposition over the nanobeam transmission. Theoretically, an MZI with two identical arms should have a flat spectrum because of the low dispersion character of silicon. However, if we integrate a nanobeam into one arm, the arm that has been treated as a control will perform the same as the

pristine waveguide, whereas the other arm will still have the same spectrum as a nanobeam transmission. As analyzed above, from the Fabry-Perot cavity model, we can predict that wave front of wavelengths at the peaks of spectrum will have same phase information, which is the same as that of inlet phase. Nonetheless, phase of the light from the control arm will have different situation. Thus, phase information will have the following equation:

$$\varphi_C = \frac{2\pi n_{Si} L}{\lambda}$$
$$\varphi_N = \frac{2\pi n_g(\lambda) L}{\lambda} \tag{13}$$

where φ_C is the accumulated phase shift after the reference arm and φ_N is the cumulative phase shift after propagating through the nanobeam arm, and $n_g(\lambda)$ is group index at target wavelength.

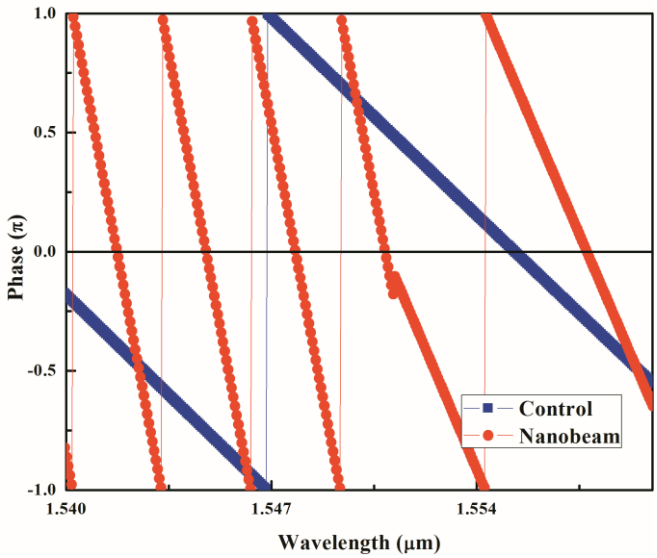

Fig. 16 Phase distribution of two arms in single armed slow light MZI

Corresponding phase information is plotted in Fig. 16. As described above, from left to right of Fig. 16, the fringe of nanobeam (labeled in red) becomes less and less dense, which reflects the decreasing of group index. Thus the superposition of electric field at different wavelengths

that are above band edge wavelength will include various phase information to make the output spectrum in the shape of Fig. 15(b). Whereas for light below band edge wavelength, the fluctuation may result from mode mismatch at the input splitting junction or bend waveguide at the non-slow light arm. Thus in order to avoid unnecessary amplitude fluctuation, we fabricated devices with larger banding radii in the round of experiment.

Theoretically, after the combination with MZI, the sensitivity should be enhanced due to interference effect. However, we did not observe an enhancement from this simulation. This is susceptibly due to the simulated physical length of MZI arms are not sufficiently long. We can assume the scenario as follows:

The spectrum from nanobeam arm has multiple peaks. In order to make it clearer, we only observe a narrow range at band edge and assume these peaks are uniformly distributed. Thus each peak corresponds that the phase at this wavelength is 2π. Contrarily, the spectrum from the unstructured arm has constant intensity as well as uniform phase distribution. Assume that the 2π phased wavelengths from nanobeam arm is n times denser than the unstructured arm. Then suppose that there is a wavelength λ_0 that is phase matched, which means a peak in nanobeam spectrum has a wavelength that also corresponds to the output phase of 2π. Now if the nanobeam spectrum shifts by x_0 and the other remains unchanged, the phase change of nanobeam spectrum at this wavelength is assumed to be $x_0/(d/n)$, where d is the distance between two 2π phased wavelengths in waveguide spectrum. At the wavelength of $\lambda_0 + x_0$, the phase at the waveguide spectrum is x_0/d and the phase information of nanobeam spectrum at this wavelength is 2π (or 0). This leads to a phase contrast of $- x_0/d$. Whereas at the wavelength of $\lambda_0+x_0+d/2n$, the phase at the corresponding wavelength of waveguide spectrum is $(x_0 +d/2n)/d$ and the phase of nanobeam spectrum at this wavelength is π. This leads to the phase contrast between two spectra is $\pi–(x_0$

$+d/2n)/d$, which equals to $\pi-(x_0/d)-1/2n$. Thus the phase matching condition will be satisfied in the range between the wavelength of $\lambda_0 + x_0$ and $\lambda_0 + x_0 + d/2n$. After derivation, the deviation between λ_0 and phase matching wavelength after spectrum shifting is:

$$\Delta\lambda = \frac{d}{2n} \bullet \frac{\frac{x_0}{d} + \frac{1}{2n}}{\pi - \frac{1}{2n}} \tag{14}$$

Since the intensity fluctuation according to interference is in the sinusoidal shape, whereas we assume the intensity of denser spectrum is in Lorentz shape due to the F-P resonance. Thus as long as x_0 is within a certain range, the spectrum shift $(\Delta\lambda)$ will be observed larger than x_0. The larger the n is the larger $\Delta\lambda$ will be. In our case, in order to increase n, one can either resort to increase the length of slow light region or enhance the group index even higher. This point is also verified according to the analysis above and the study below (rectangular hole structure). Thus the simulated result demonstrates the same in the spectrum shown above is probably due to the short length of slow light region. Thus, the shift reflected from the spectrum mainly comes from the band diagram change due to index change, whereas interference is not yet the major factor.

After converting this spectral sensitivity (140nm/RIU) into phase sensitivity, we have the band edge phase sensitivity as high as 117,000rad/RIU-cm, which is 8 times higher than other integrated MZI biosensing reports.

The last step for this model is two identical arms both integrated with same structured nanobeam device. Compared to single armed MZI, this type of MZI will put out same phase information as long as the wavelength remains the same. To take the peak that is nearest to the band edge (around 1.539μm) as an example: the output phase for this wavelength is supposed to

be 0, while the other arm has the same situation. Thus light from two arms satisfy constructive interference condition. However if only one arm is applied index variation treatment, this spectrum will reddishly shift. At this time, the original peak wavelength will have a non-zero phase contrast compared to phase information from another arm, which means the complete constructive interference relation is no more satisfied. This leads to the intensity of light at this wavelength suffer from both the intensity attenuation due to Fabry-Perot effect and destructive interference. Reflecting into the spectrum, this effect should assist in light intensity variation. This means that when reacting to the same index variation, this dual armed MZI will have lower LOD from the aspect of intensity observation, since the intensity variation is larger than the previous two models. Hence by applying the mostly same model as the previous one, but both arms are holey structured waveguide, we change the index of air holes and surroundings at one arm into 1.001 and obtain results illustrated in Fig. 17.

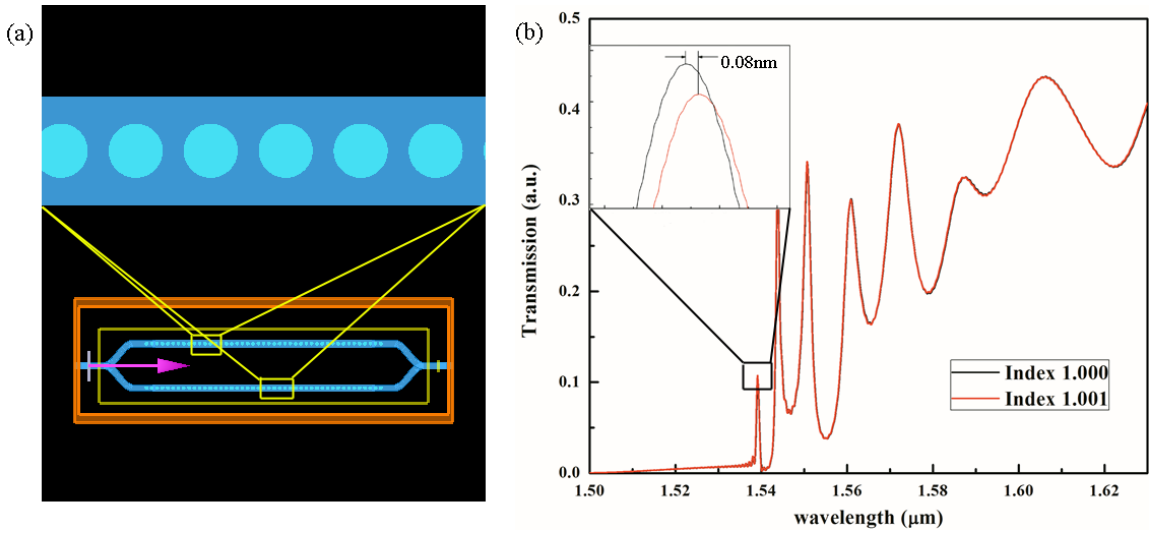

Fig. 17 (a) Dual armed MZI model in FDTD environment; (b) Transmission spectrum and shifted spectrum of dual armed MZI devices

As observed in the inset of Fig. 17 (b), we can see that the shift of dual armed is actually not as high as the single armed MZI. We will attribute this to the merging of two peaks from two arms. Since after asymmetric treatment to two different arms, shift from the sensing arm will superposition on the control arm. By comparing the intensity only, if the perturbation is minor, the slightly split peak will merge into a broader peak since the superposition of two close peaks will result in the maximal intensity occur in the middle and the actual shift from one arm will be concealed in the shift of large peak shift. However, as predicted above, this peaks has phase information as well. Once the phase matching condition has been broken, the intensity will drop due to destructive interference. That is the reason why the spectrum shift is even less than single MZI sensors.

From another point of view, due to the derivation of our single armed MZI scenario, peak deviation ($\Delta\lambda$) is less than x_0 result from n=1. Due to this, the phase sensitivity of dual armed MZI drops from 117,000 rad/RIU-cm to 67,000 rad/RIU-cm.

As predicted, although the shift is not as high as previous single arm MZI or nanobeam device, the LOD will decrease. From the graph, we can tell that the shifted peak has larger intensity contrast compared to previous situation. Note that the major ticks on vertical axes in insets of Fig. 15 and Fig. 17 stand for 0.01 a.u. The intensity of each spectrum is normalized to input signal incident. Since the LOD is demonstrated as the minimum variation that can be regarded as device spectrum shifting. Assuming the output signal from measurement system has the same standard deviation, the LOD from the point of intensity variation is enhanced.

Apart from round holes, we also investigated rectangular holes as well as diamond holes. The reason that we selected these shapes is based on the consideration of the operation of electron-beam lithography: it is orthogonally binary operation. The electron gun typically can move in

two orthogonal directions instead of curving around. Technically, fabrication of round holes is actually dividing round holes as polygons with many sides. Once the round hole is not in perfect shape, it will cause some scattering while the light is propagating, which is undesirable. Thus our study of shape is providing the fabrication an easier process. The corresponding structures and band diagrams are illustrated in Fig. 18. By sticking to the same principle of fixing the operation wavelength at 1.55μm, and feature size is no less than 100nm, most of the dimension remains the same (such as the width of waveguides and nanobeam lattice constant). All parameters that we tuned are holes' dimensions. After calculation, we set the rectangular hole size to be 300nm by 200nm, whereas the size of diamond holes are fixed to be 200nm on each side.

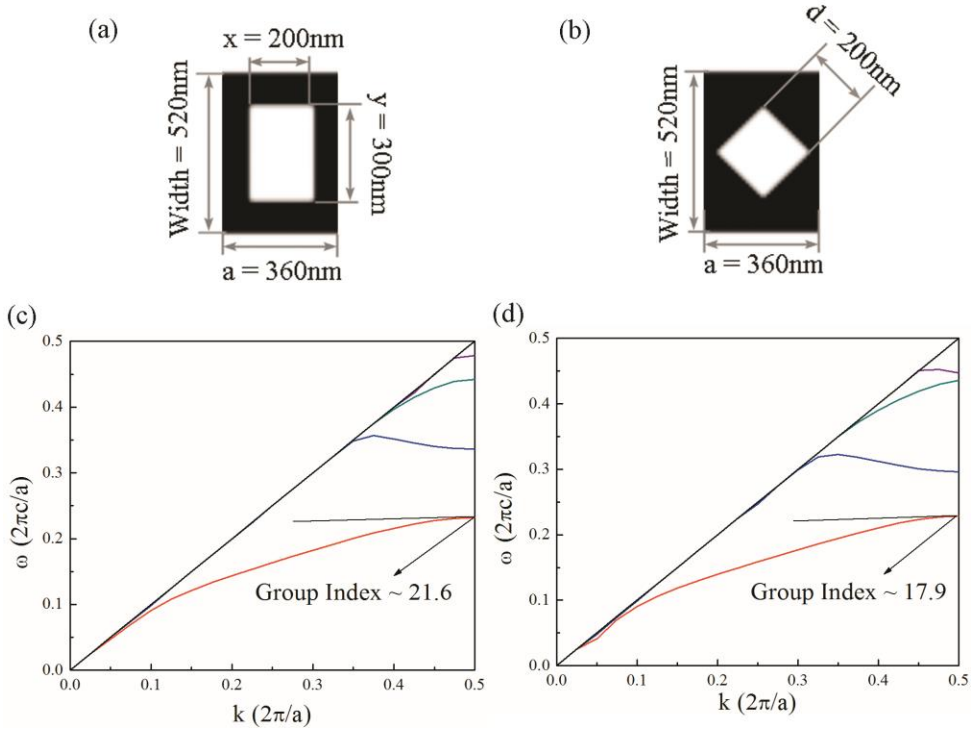

Fig. 18 (a) and (c) The lattice cell of rectangular hole nanobeam structure and its band diagram; (b) and (d) The lattice cell of diamond hole nanobeam structure and its band diagram

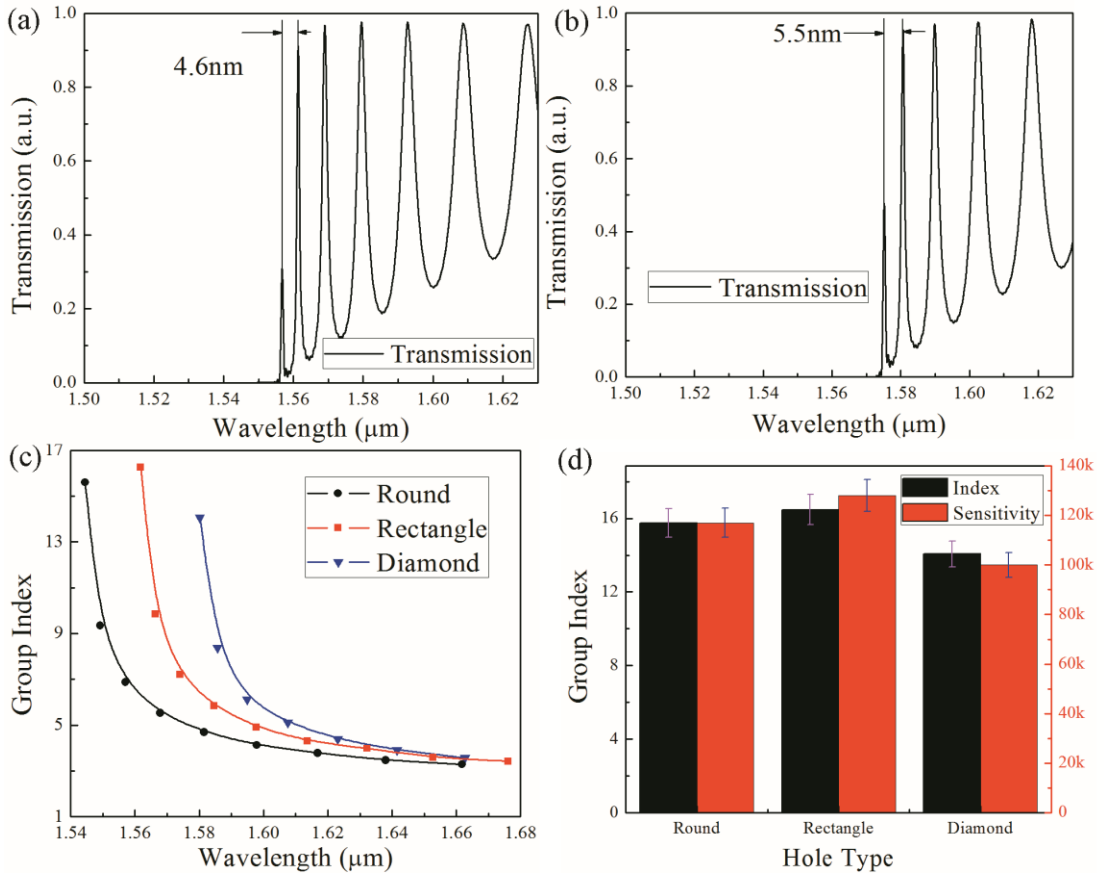

Fig. 19 (a) Transmission spectrum of rectangular hole nanobeam; (b) Transmission spectrum of diamond nanobeam; (c) Group Index contour for 3 types of nanobeams; (d) Sensitivity and group index comparison for 3 types of nanobeams

Same as the calculation for round hole, we also simulated this structure using FDTD software, and transmissions as well as corresponding group index contour are sketched in Fig. 19. Most study of these two structures are conducted with the same methodology as those of round holes, thus we listed a table (Table 1) that includes sensitivity information for three structures and plotted in Fig. 19 (b). Here we only listed the phase sensitivity of single armed MZIs, because they demonstrate either the best performance of sensitivity compared to double-armed MZIs and nanobeams or the best potential compared to all reported publications. As we can observe from Fig. 18 (c) and (d), the rectangular holes' structure has the highest group index and the highest

group index from band diagrams occurs at the rectangular case, which is approximately 16.5. This shape concerned variation should be attributed to the spacing between two adjacent rectangles. Since we selected to use silicon mode to support the propagation, of which electric field mostly should distribute within silicon region, as illustrated in Fig. 12. Thus the structure with larger spacing between holes should have higher potential for confining energy inside the corresponding region. Thus from this point of view, the diamond holes has the smallest group index, which is 14.1 is reasonable.

Table 1 Sensitivity performance for 3 slow light structures

	Highest Group Index	Nanobeam	Single Armed MZI		Dual Armed MZI
		Spectral Sensitivity (nm/RIU)	Spectral Sensitivity (nm/RIU)	Phase Sensitivity (rad/RIU-cm)	Spectral Sensitivity (nm/RIU)
Round	15.75	140	140	117,000	80
Rectangular	16.47	140	150	128,000	70
Diamond	14.06	140	140	100,000	60

Note that all highest group index in the table are calculated from transmission spectrum but not band diagram. According to the table above, we can clearly tell that when group index is larger, which functions as longer device region, single arm MZI will place more and more weight on the total spectrum shifting. Compared to rectangular cases, diamond structure still has comparable sensitivity in both nanobeam scenario and single arm MZI case. Whereas the dual armed MZI shifting tell us that dual arm MZI peak broadening effect is consistent with the device group index. By converting sensitivities of each case into phase sensitivity, we can have 117,000rad/RIU-cm, 128,000rad/RIU-cm and 100,000rad/RIU-cm for single armed MZI for the round, rectangular, and diamond hole topology, respectively. Thus by plugging slow light factor

($\Delta\lambda$) into spectral sensitivity, we can tell that the higher the group index is, the higher phase sensitivity there will be.

2.2 Defect Hole Slow Light MZIs

Above are basic slow light MZIs design studies. Whereas the next section will discuss about novel MZIs that we proposed for even higher sensitivity: Multi-Hole Defect Slow Light MZI. Our group has reported MHD photonic crystal cavity biosensor which demonstrated higher sensitivity compared to previous approaches [19,46]. In the following section, we demonstrated a defect hole integrated slow light waveguide structure combined with MZI for biosensing application.

From the study above, we emphasized that we selected silicon mode to make waveguide less lossy, which actually makes light confined more within silicon region. According this character, we can introduce small defect holes in between two adjacent regular holes. In this way, the electric filed energy confined within silicon region is squeezed out into defect holes. Due the continuity of the electric field at the surface of two different dielectric media, the electric field intensity will be much higher than conventional situation.

Sticking to the principle of maintaining the center wavelength located at 1.55 μm, we need to enhance current structure's period. Thus we choose to enhance the spacing between two regular hole both for modifying filling factor and leave enough space for defect holes to satisfy design rules (spacing rules). On the other hand, due to there is not enough room for defect hole in between the spacing of adjacent lattice holes, we did not conduct the diamond hole device with defect hole.

After tuning, we fixed the period to be 410nm, whereas the size of round holes remains to be the same and rectangular holes will have 20nm and 50nm extension on x and y directions, respectively. Practically, RIE fabrication process is to etch away silicon not protected by the resist, the design rules of minimal spacing size is less restricted. This is because the silicon ridge (for example, the spacing between lattice holes) is the remainder after the hole pattern has been etched. Therefore, as long as the hole size is achievable, the pattern can be managed to fabricate. Thus we set the defect hole with the diameter of 100nm. Finally, the band diagrams and corresponding profile of these structures are illustrated in Fig. 20.

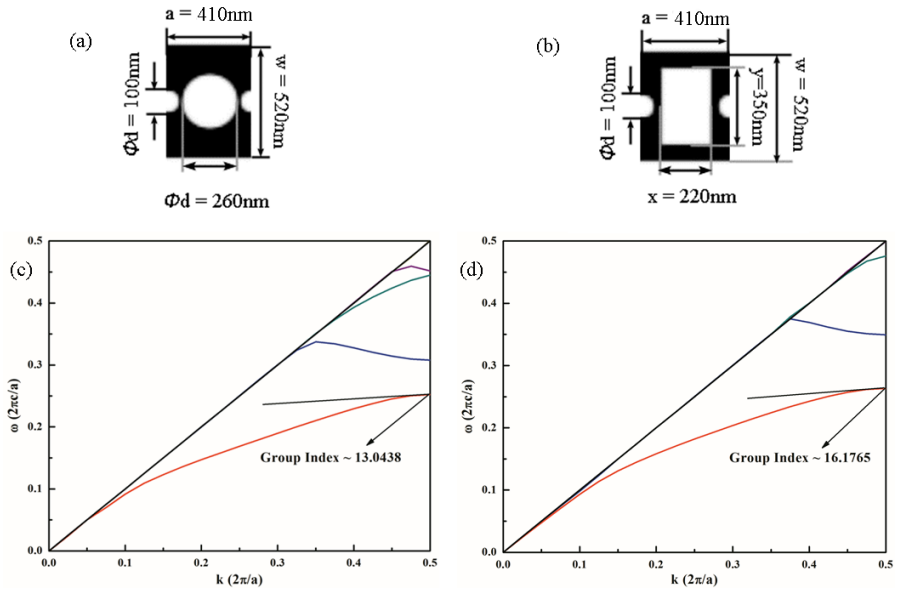

Fig. 20 (a) and (c) The lattice cell of round hole nanobeam with defect hole structure and its band diagram; (b) and (d) The lattice cell of rectangular hole nanobeam with defect hole structure and its band diagram

Comparing the group index performance to those structures investigated above, we observed a decrease in group index, which is 13.04 and 16.18, respectively. Generally, the smaller period of slow light waveguide is the larger group index this waveguide will have. Because intuitively, assuming the operation wavelength (λ) fixed, the band edge point of silicon mode band diagram

should be a/λ, where a is the lattice constant. If a decreases, the band edge point will correspondingly decrease, which means the band diagram for silicon mode will bend down closer to x-axis. Bending down of silicon mode will make the curve generally more flat, which will result in higher group index. This is the reason why the group index experienced degeneration after increasing the periodicity.

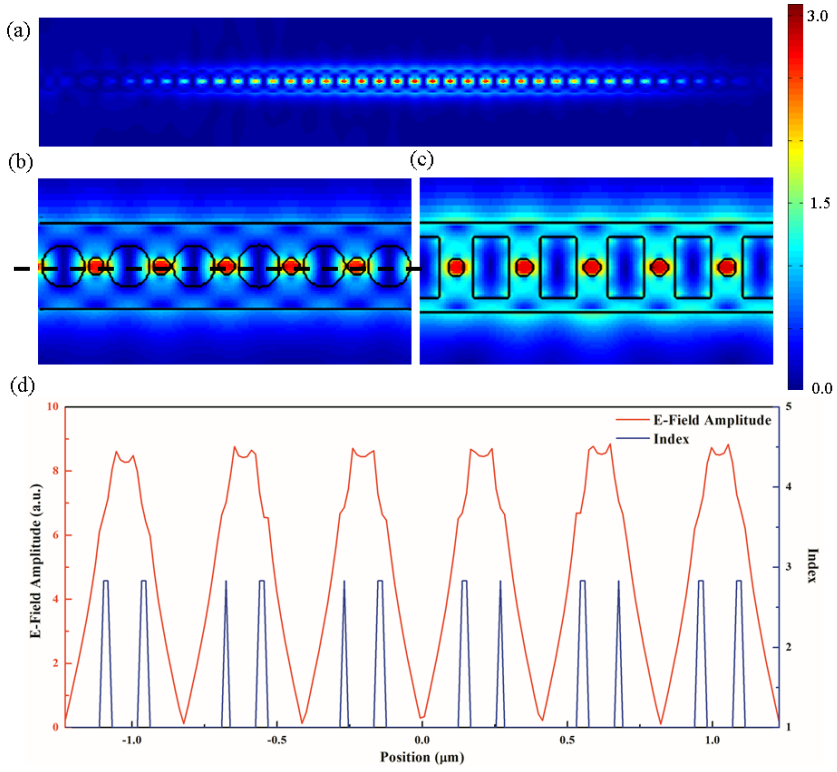

Fig. 21 (a) Eletric field distribution of round hole nanobeam with defect holes; (b) Zoomed in field distribution of round hole nanobeam with defect holes; (c) Zoomed in field distribution of rectangular hole nanobeam with defect holes; (d) Sliced field distribution at dashed line in (b)

By applying these structures into FDTD simulation, we can draw the electric field distribution for round hole structure and rectangular hole structure in Fig. 21 (a) - (c). Fig. 21 (d) is the sliced field distribution of dashed line in Fig. 21 (b). We can tell that the electric field is well confined inside the defect holes with much larger intensity due to electric displacement

continuity. Thus, intuitively, we can tell this field confinement will promise much higher sensitivity because of higher LMI. Furthermore, in Fig. 22, we showed FDTD simulated transmission spectrum and group index contour for both structures. Apart from that, the group index trend for each structure is consistent with the calculation of band diagram. The difference between band diagram calculation and FDTD simulation may come from different meshing grid. We designed the length of slow light waveguide to be the same, which is 16 μm, to eliminate the sensitivity affect caused by the length of slow light region. In the case of 410nm as lattice constant, the number of period of devices decreases from 45 to 40.

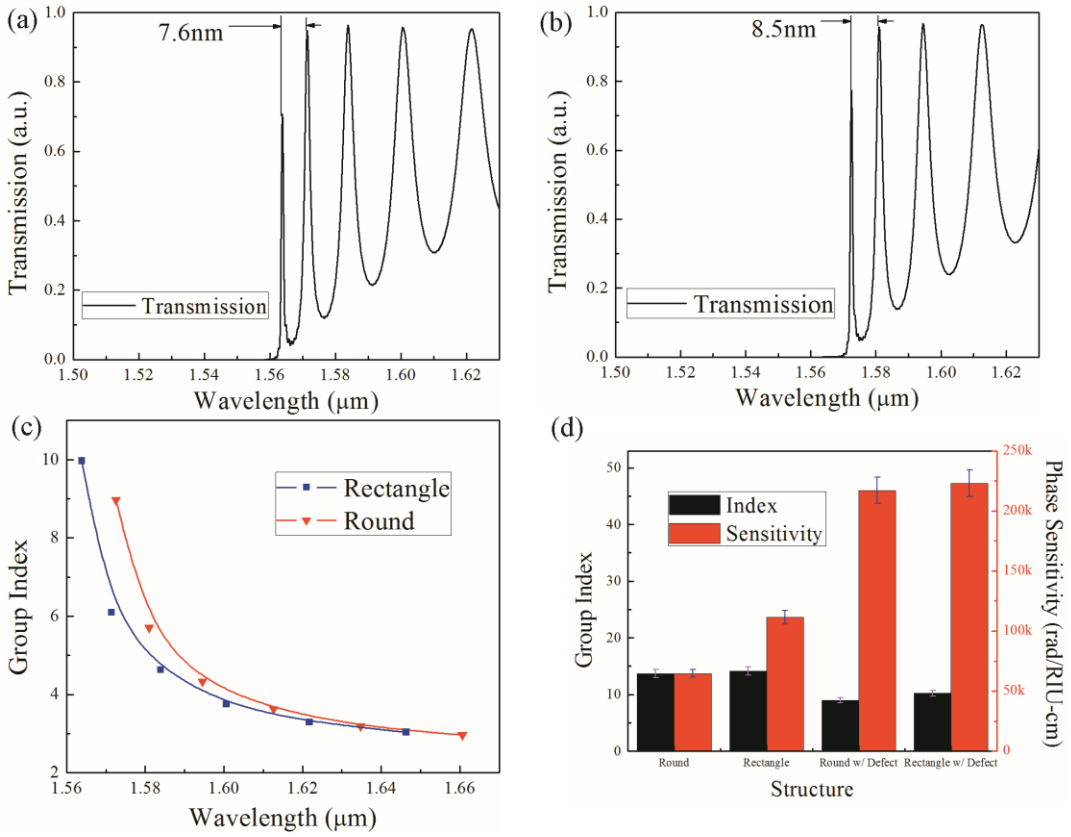

Fig. 22 (a) Transmission spectrum of defected round holes nanobeam; (b) Transmission spectrum of defected rectangular holes nanobeam; (c) Group index contour of both nanobeams; (d) Comparison of the sensitivity of defect hole single armed MZIs

Same as previous study methodology, nanobeam only, single armed MZI and dual armed MZI were studied for sensing usage. For the concern of comparing similar devices, we also calculated the baseline devices simply by removing all defect holes. The reason that we also set this baseline as a control is to verify how much the introduction of defect hole will affect the sensing performance of our slow light MZI devices. To avoid posting repeating information, we did not include band diagram or transmission spectra for these control devices. But some data will be mentioned in text or table. After series of simulation, all data are processed to list in Table 2.

Table 2 Sensing performance of MHD slow light MZIs

	Highest Group Index	Nanobeam	Single Armed MZI		Dual Armed MZI
		Spectral Sensitivity (nm/RIU)	Spectral Sensitivity (nm/RIU)	Phase Sensitivity (rad/RIU-cm)	Spectral Sensitivity (nm/RIU)
Round	13.69	160	140	64,600	70
Rectangle	14.11	200	210	116,000	120
Defect w/ Round	8.97	450	470	217,000	260
Defect w/ Rectangle	10.21	410	430	223,000	260

By comparing group indices of these devices, we can tell the introduction of defect holes will lead to group index reduction, which is as predicted above, due to the lattice constant increases as well as filling factor drops for defect hole cases. Compared to round holes with defects structure, rectangular holes with defects nanobeam presents larger group index.

However by changing environment index by 0.001, we observed that the conventional round hole device has comparable shift compared to the study from last section. This is because the operation wavelength is in the range of 1.65 – 1.75μm, which makes the mode less confined

within the silicon waveguide. In turn, this weak confinement will make the LMI larger, leading to the comparable spectral shift from the last section. However, the phase sensitivities of these non-defected newly designed devices are less than previous structures which has the period of 360nm. This indicates that the higher group index a structure has, the better phase sensitivity performance a structure will have.

Whereas vertical comparison let us know that defect hole devices do makes the sensitivity much larger. Thus, by calculating the best case, which is defected rectangular hole single armed MZI device, can reach phase sensitivity as high as 223,000 rad/RIU-cm, which is 15 times higher than reported MZI devices without sacrificing the compactness of a device, twice higher than its baseline case listed in Table 2. Compared to the non-defect case in Table 2, the phase sensitivity of defect cases are twice as large as non-defect cases. Even compared to the results we have from last section, the phase sensitivity is twice larger. This indicates that compared to slow light effect caused field enhancement, LMI plays a more important role in the optical biosensing technique.

However, one drawback of this design is the sacrificing ease of feature size fabrication. According to models we applied above, the feature size of defected round hole is only 25nm, which will make the fabrication process extremely challenging. Whereas the case of rectangular holes, the feature size is around 50nm, which is also hard to control. Thus this introduction of defect holes also introduces a tradeoff between fabrication process and desired sensitivity.

Chapter 3: Device Fabrication

3.1 Slow Light MZI Fabrication

Fabrication precision is a key element in obtaining decent slow light waveguide. Although the photonic crystal theory was proposed as a hypothesis by Yablonovitch et al. in 1980s [62], the fabrication was not prevalent until early this century due to the critical condition for fabrication feature size down to 200nm to 400nm. This size of details is crucial for opening up the predicted PBG at optical wavelengths.

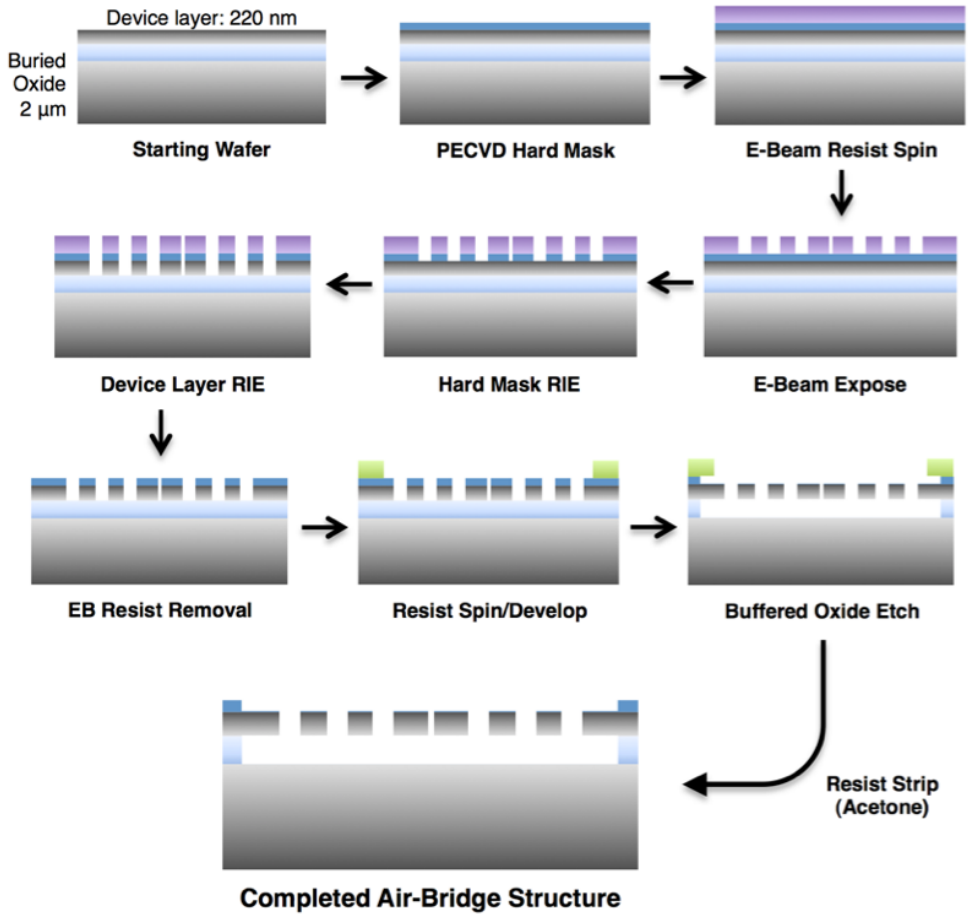

Fig. 23 Flowchart of electron-beam lithography based fabrication of nanobeams [63]

The fabrication of 1D photonic crystal (nanobeam) and 2D photonic crystal complies with mainstream semiconductor CMOS fabrication techniques, shown in Fig. 23. We applied silicon-on-insulator (SOI) as wafer for fabrication. SOI is a three layered wafer consist of one buried oxide layer (BOX) sandwiched by upper silicon layer and silicon substrate. They are commercially available on several specific thickness of upper silicon layer (220nm, 270nm, 340nm, etc.). This is because these thicknesses are typically in numbers of $\lambda/2n$, where λ is wavelength in vacuum, n is refractive of silicon. Because the telecommunication wavelength range from 1.3μm to 3μm, the typical thicknesses for research are listed above. Due to large index contrast between silicon and oxide layer, this thickness is sufficient for supporting the TE0 mode. For the buried oxide layer, it has the thickness varies from 1μm to 3μm to provide index contrast as well as enough stiffness for whole device.

In our case, the 220nm type was applied for further study. A thin layer of resist is firstly spin-coated to the surface of SOI. Two main kinds of resists used for electron-beam lithography are ZEP520A and PMMA. Typically, when using PMMA, an oxide hard mask will be in need due to the low selectivity for PMMA resist during the RIE process later.

Next, photonic crystal lattices along with connected waveguides are exposed under electron beam in the same step with high precision. Here the single step characteristic can only be applied to through etching devices. If the designed devices are in shallow etched shape, e. g. ridge waveguide, whereas the grating coupler or TE mode micro-ring resonator are through etched, two steps of fabrication will be needed. First exposure step is applied to shallow etched regions, the second is for fully etched step. For shallow etched devices, alignment step between two exposures is necessary. This will make the fabrication throughput much less. Thus most

industries prefer to integrate full etched or uniformly shallow etched devices instead of non-uniform heighted structure.

The following step is developing. This is to dissolve away the polymer of resist whose crosslink has been broken by electron beams. After this step, the resist will be patterned and shaped. Followed by reactive ion etching (RIE) step, the pattern is transferred into upper silicon layer. This etching process will automatically cease due to the plasma reaction with silicon dioxide is much slower than that with silicon. However, over dosage of RIE will make the sidewall slightly sloped, which is undesired.

After O_2 plasma cleaning, the residual of uncured resist is removed from the surface of device. This is the target device fabrication process for most devices.

Nevertheless, in some cases, a further step of undercutting is needed to enable the waveguide support symmetric mode. In this method, the upper silicon layer will be suspended by etching away silicon oxide underneath the upper silicon. This suspension step is sometimes crucial for opening up a PBG within photonic crystal structure. Moreover, larger surface area and better confinement within silicon waveguide are also preferable advantages from this technique [64]. The etching process is implemented using buffered oxide etchant (BOE). Firstly, a layer of photoresist is spin-coated on the surface of samples. Desirable thickness of photoresist is around 1.3μm. That is because too thick resist will result in slanted sidewall and pattern expansion due to light diffraction at the edge of mask, whereas too thin resist will be easily peeled off when in touch with BOE. Then windows (over the photonic crystal devices) are opened using photolithography. Undesired regions are covered using chromium mask to block UV light. After developing, only the device regions are exposed to the air via those windows. The sample is then soaked in BOE. It is a buffered solution containing HF that can dissolve silicon oxide. Thus BOE

will isotropically etch away regions of BOX layer where exposed to BOE, even they are originally beneath silicon layer. Then a suspended photonic crystal device is fabricated. However, as mentioned above, removing the BOX layer will reduce the robustness of devices. Fabricated devices are shown in Fig. 24.

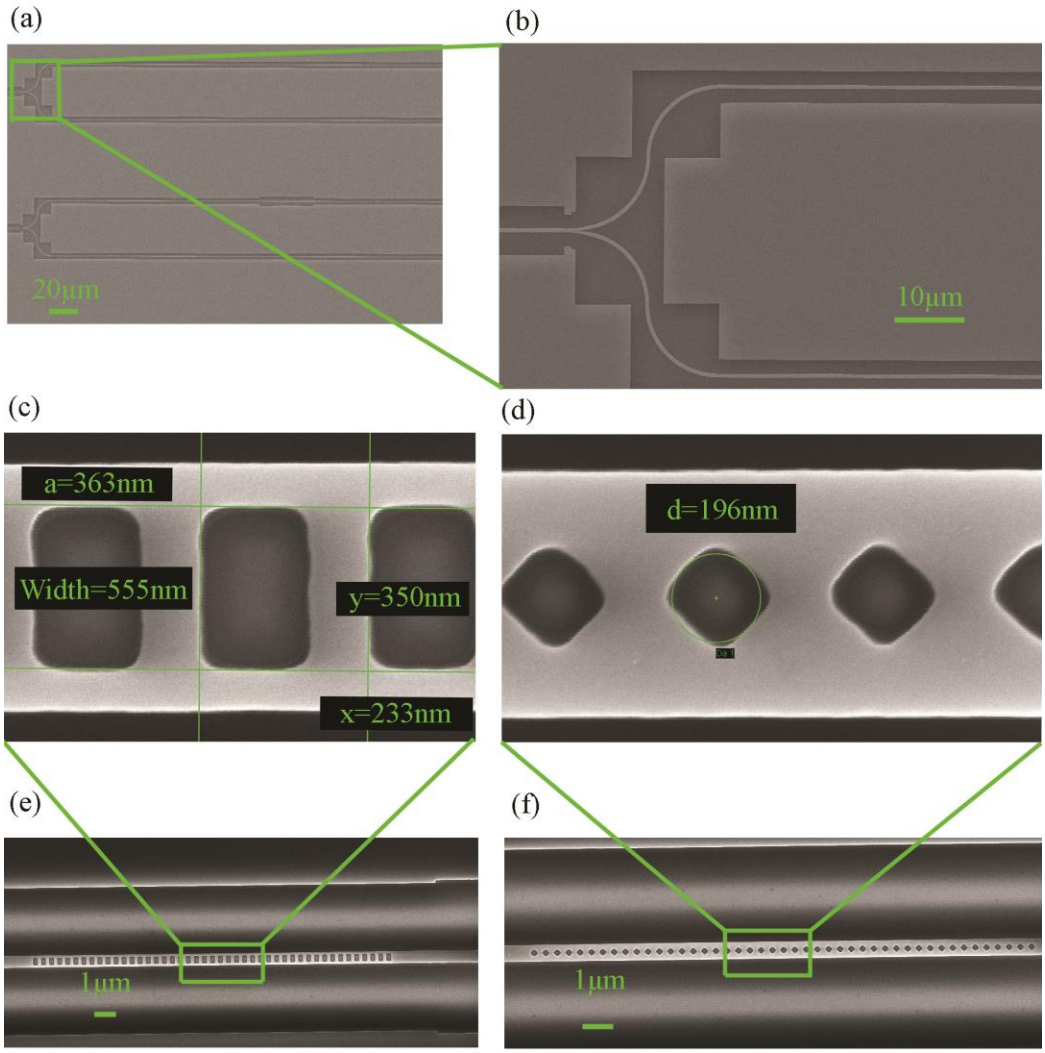

Fig. 24 (a) SEM image of the top view of MZI devices; (b) Zoomed in image of MZI junction; (c) Zoomed in image of rectangular holes; (d) Zoomed in image of diamond holes; (e) Image of slow light waveguide with rectangular holes; (f) Image of slow light waveguide with diamond holes

Fig. 24 (a) and (b) are SME images for MZI devices and zoomed in image of MZI junction. In Fig. 24 (c) and (e) are the SEM images of fabricated rectangular hole nanobeam and MZI devices. From the ruler tools inside the image, we can tell the dimension of rectangular hole nanbeams are larger than expected. Since fabrication process is a balance between etching budget and dosage, which means that the pattern we drew for fabrication should be designed to be slight smaller than expected. On the other hand, dosage stands for the standing time of electron gun at each specific location. Thus if these two elements are not balanced, the dimensions will turn out to be different from design. Fig. 24 (d) and (f) are SEM images for diamond hole devices. These devices are more decent in dimension compared to rectangular hole devices. We can tell from the images that for each holes, the corner is not perfect sharp. That is because of proximity effect, an effect that will occur at the junction of two sides. Since electron beam is not focused perfectly at a spot but distributed in the form of Gaussian function, thus for those regions that are not supposed to be exposed are not necessarily free from exposure. This led to the deformation of patterns. Unfortunately, we did not fabricate round hole or defected round hole devices. This will be included in future works.

When it comes to Fig. 25 (a) and (b), we can see that the defect holes are larger than expected, which makes the pattern seems to work like a pinch waveguide [65] instead of slow light waveguide. This is because we intentionally applied larger dosage at the regions of defect holes. Since when the region of desired pattern is too small, one step of EBL movement will not guarantee the proximity effect to be confined inside the area of that pattern. So we decided to utilize larger dosage to assure the hole can be opened. However, from the SEM images, dosage is one factor that makes the size of devices off dimension.

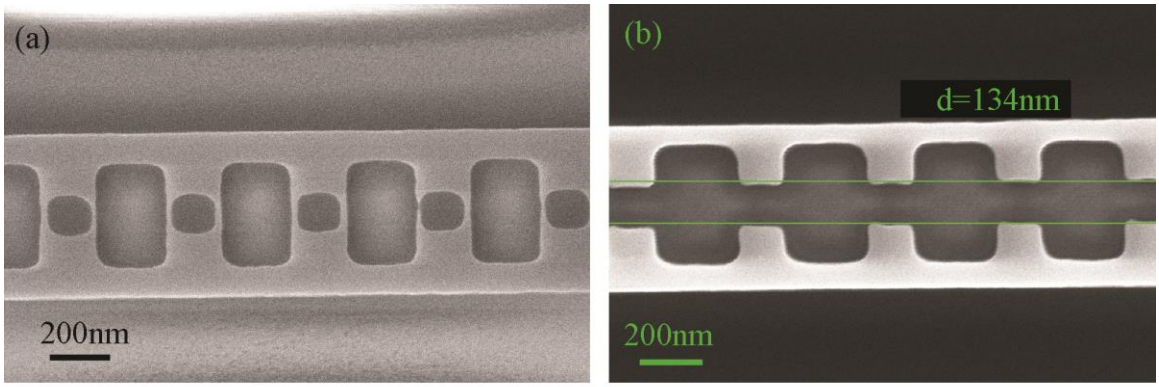

Fig. 25 (a) MHD based slow light waveguide; (b) Failure sample for defect hole fabrication

3.2 Microfluidic Fabrication and Optimization

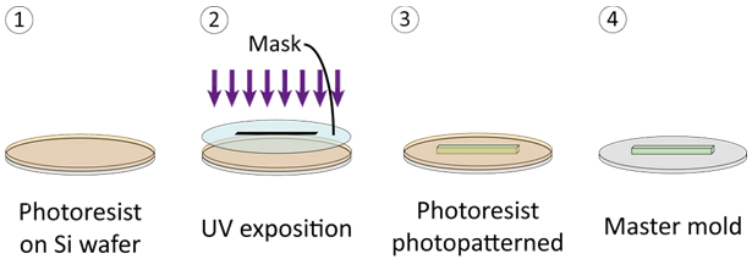

Fig. 26 Standard SU-8 mode fabrication process (Figure from Ref. [66])

In this section, we briefly introduce the definition and classic fabrication process of microfluidic system. On one hand, microfluidics can help to manipulate tiny volume of chemical or solvent. On the other, it will protect from most solvent from evaporating from the flat surface. Due to these advantages, we applied microfluidic system to the surface of our fabricated device for bulk sensing. In this way, more types of solvents can be tested disregarding the evaporation effect. A traditional microfluidic fabrication process starts from the fabrication of the master mold, as illustrated in Fig. 26 [66].

Starting from the first step of fabrication, which is SU-8 master mold fabrication. Master mold consists of patterned SU-8 micro-channel on silicon wafer. Alternatively, pure silicon channel can also be made for master mold by applying Reactive Ion Etching (RIE) technology. SU-8 mold fabrication process is basically based on photolithography technology. A layer of SU-8 that corresponds to the target thickness is spin-coated on the silicon wafer. For a thickness of 100μm, the spin-coating speed is set to be 1650RPM with the usage of SU-8-2050. After pre-baking the silicon wafer for 5min in 65℃ and 20min in 95℃, two ultraviolet exposure steps are applied. The energy of exposure is 160J. This pre-baking process involves drying the SU-8 resist after spin coat by removing its excess solvent to stabilize the resist film. Then a 1min under 65℃ and 10min under 95℃ post-baking process is applied to reduce the standing wave effect with the mechanism of photoactive compound diffusion. With approximately 1min developing after cooling down of the sample, the pattern should be bonded to the silicon wafer.

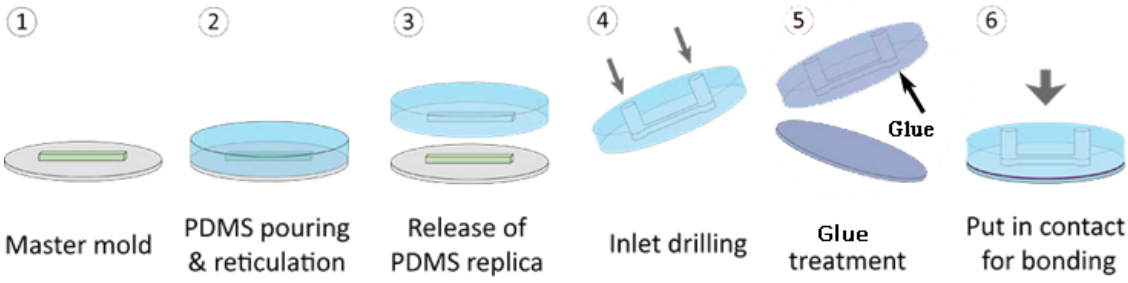

Fig. 27 Microfluidic system fabrication process (Figure from Ref. [66])

The second step of microfluidic fabrication is to pour PDMS onto master mold, as indicated in Fig. 27 [66] to obtain patterned channel shell. The PDMS used in this step is the mixture of pure PDMS and curing agent with the ratio of 10:1. After degasing poured PDMS in vacuum chamber, the PDMS sample is baked in the oven under 65℃ for more than 4hr.

Cured PDMS replica is cut out using scalpel. Holes are punched at the ends of each channel on PDMS replicas by using corresponding sized puncture. After that, smearing a layer of glue to the interface of PDMS replica is followed by a step of contacting the interfaces. The glue used here is mixture of PDMS and curing agent with the ratio of 2:1.

Furthermore, we clamped the sample together with the PDMS replica using a stage designed and then baked under 60 ℃ for more than 4hours, demonstrated in Fig. 28.

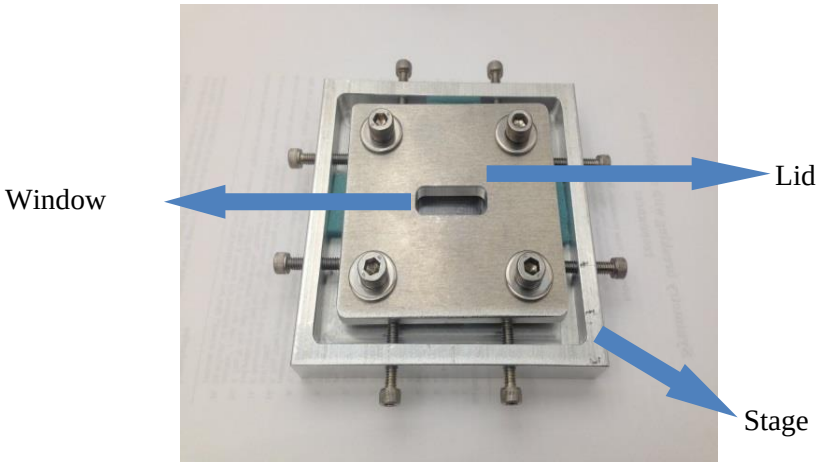

Fig. 28 Stage designed for microfluidic system fabrication

After applying mixture to substitute pure curing agent as glue, one can observe that PDMS does not peel from the corner any more. Since we have applied a layer of glue to the interface of these two samples, the mechanism of attachment is no longer the chemical bonding as mentioned before, but the adhesion of PDMS and SOI sample using the curing agent and PDMS mixture. Finally, the total device after this technique is shown in Fig. 29.

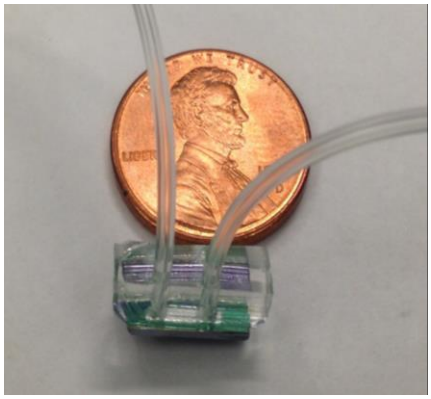

Fig. 29 Prototype of fabricated microfluidic system

Other than this, another major modification we made compared to previously applied recipe in the laboratory is the metal pin technique. Apparently, for the device above, the tubing is consuming too much space on chip. Thus, according to [67], we applied a tip sharpened needle with size of Gauge 20 to punch the PDMS, and then inserted either gauge 21 or larger metal pins as a connector between Tygon tubing and PDMS shell. In this way, more inlets and outlet can be integrated on a unit area. Moreover, the stiffness of metal pins will make them much easier to be inserted into PDMS without deforming it too much. The only drawback of this method is the weight of metal pins. But applying shorter pins will solve this issue. The final device is shown in Fig. 30.

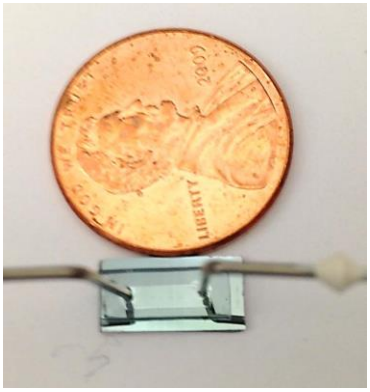

Fig. 30 Final microfluidic system with metal pin connection

Chapter 4: Experimental Results

4.1 Device Characterization

After PDMS attachment, as described in Chapter 3, the devices are characterized on the optical measurement setup shown in Fig. 31. Light is conducted out from a tunable laser (SANTEC TSL-510), of which the tuning range is from 1500nm to 1630nm. After polarization controlling, incident light end up with a lens fiber at the right hand side of the setup. Light coupled from lens fiber into chip will interact with devices. Then the output signal is collected by another lens fiber that is connected to an optical power meter (OPM). By sweeping the wavelength with tunable laser and collect all the power data from the OPM with a PC will obtain the device spectrum.

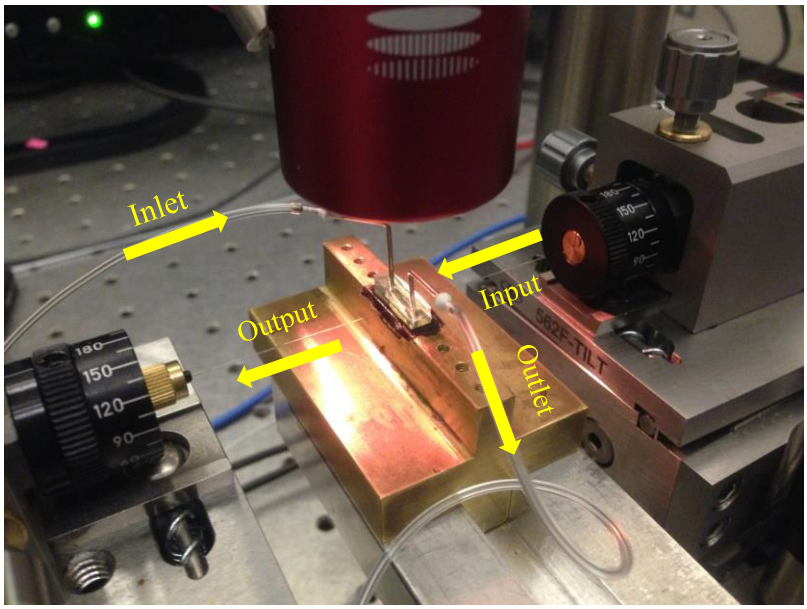

Fig. 31 Photonic devices measurement setup

Thus by measuring the devices' transmission spectra, we obtained the following spectrum for the diamond hole nanobeam as shown in Fig. 32 (a). From reading the information of the output fringe, we extracted the group indices and plotted in Fig. 32 (b). We can tell that the actual device performance is very similar to the result we have simulated using FDTD method in Fig. 19 (b). The highest group index is read as 28.8, which is higher than expected because the device filling factor is a little bit larger than simulated scenarios.

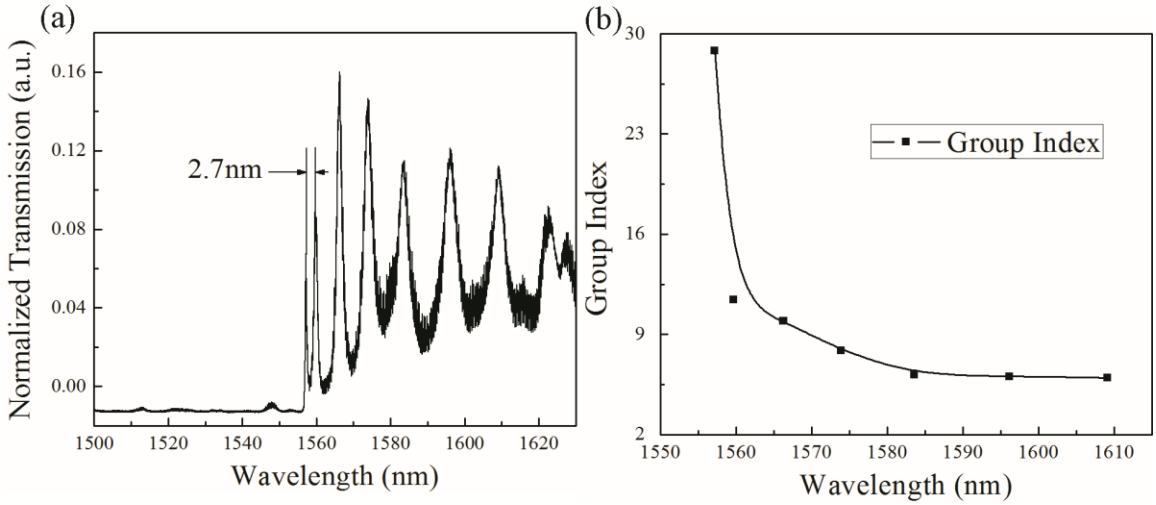

Fig. 32 (a) Measured transmission spectrum of diamond hole slow light devices; (b) Group index of fabricated devices

Other than nanobeam devices, we have also measured the single armed MZI devices and dual arm MZI devices. Their spectra were plotted in Fig. 33 (a) and (c). By measuring the location of band edges from each diagram, we can evaluate the dimension of each device to see the fabrication repeatability. Exactly due to this issue, identical armed MZI is less frequently seen for research. As we can see from the sensitivity during previous study, dual armed MZI sensors also suffer from sensitivity issue. Thus in the following experiment, we did not measure those dual armed MZI for studying. Fig. 33 (b) stands for the simulated spectrum just for the

purpose of comparison. From the comparison, we can tell the simulation fits the actual device performance.

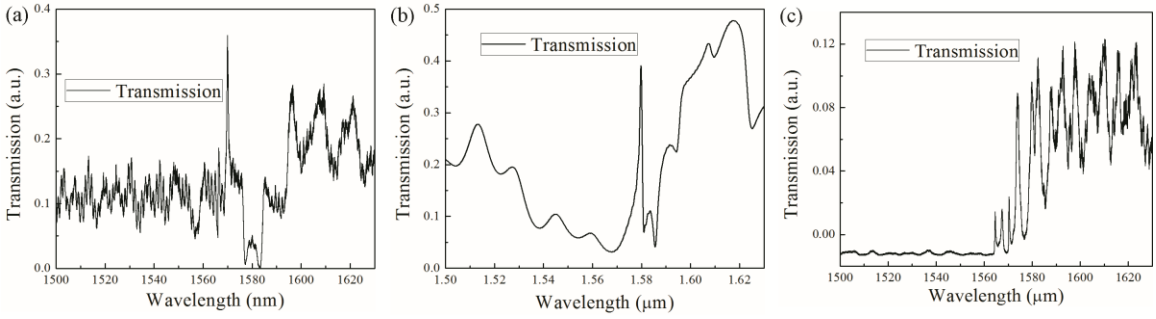

Fig. 33 (a) Measured transmission spectrum of single armed MZI with diamond holes; (b) Simulated transmission spectrum of single armed slow light MZI with diamond holes; (c) Measured transmission spectrum of dual armed slow light MZI with diamond holes

For those rectangular hole devices, we measured using the same measurement setup, but light source was substituted by a broadband white light LED, meanwhile the OPM was replaced by an Optical Spectrum Analyzer (OSA). OSA will decipher the spectrum information from collected light by Fast Fourier Transformation. The advantage of this method is the range of spectrum is very broad, since the light source is from 1300nm to 1650nm, whereas the OSA has spectrum from 1200nm to 1800nm, which is sufficient to support our measurement. However, the drawbacks of it are the sweeping time for OSA is very slow to achieve high wavelength resolution and it can only save 1000 data points for each spectrum. Since the dimensions of rectangular holes are too large, the band edge may fall into 1400nm – 1500nm, which can only be measured using this method. And the output data from OSA are plotted in Fig. 34. We can evaluate from the fringe of nanobeam to extract the group indices, which are also plotted in Fig. 33. As from the group index information, we know that the rectangular hole nanobeams do have higher group index than diamond hole structure, whose highest index is 35.5. Also, for Fig. 34 (c), we can see a clear power drop at the right side of the spectrum. This is not the band gap for

device but the gap for LED source. Since this LED source is actually three LED that is complementary to each other's spectrum, so 1470nm is near the gap between two main peaks. This is another drawback of this method. Therefore in the following sections, unless mention specifically, most data will be based on diamond hole structures only. Fig. 34 (d) shows the simulated spectrum of single armed MZI with rectangular lattice holes, which demonstrates the simulated spectrum shape at band edge.

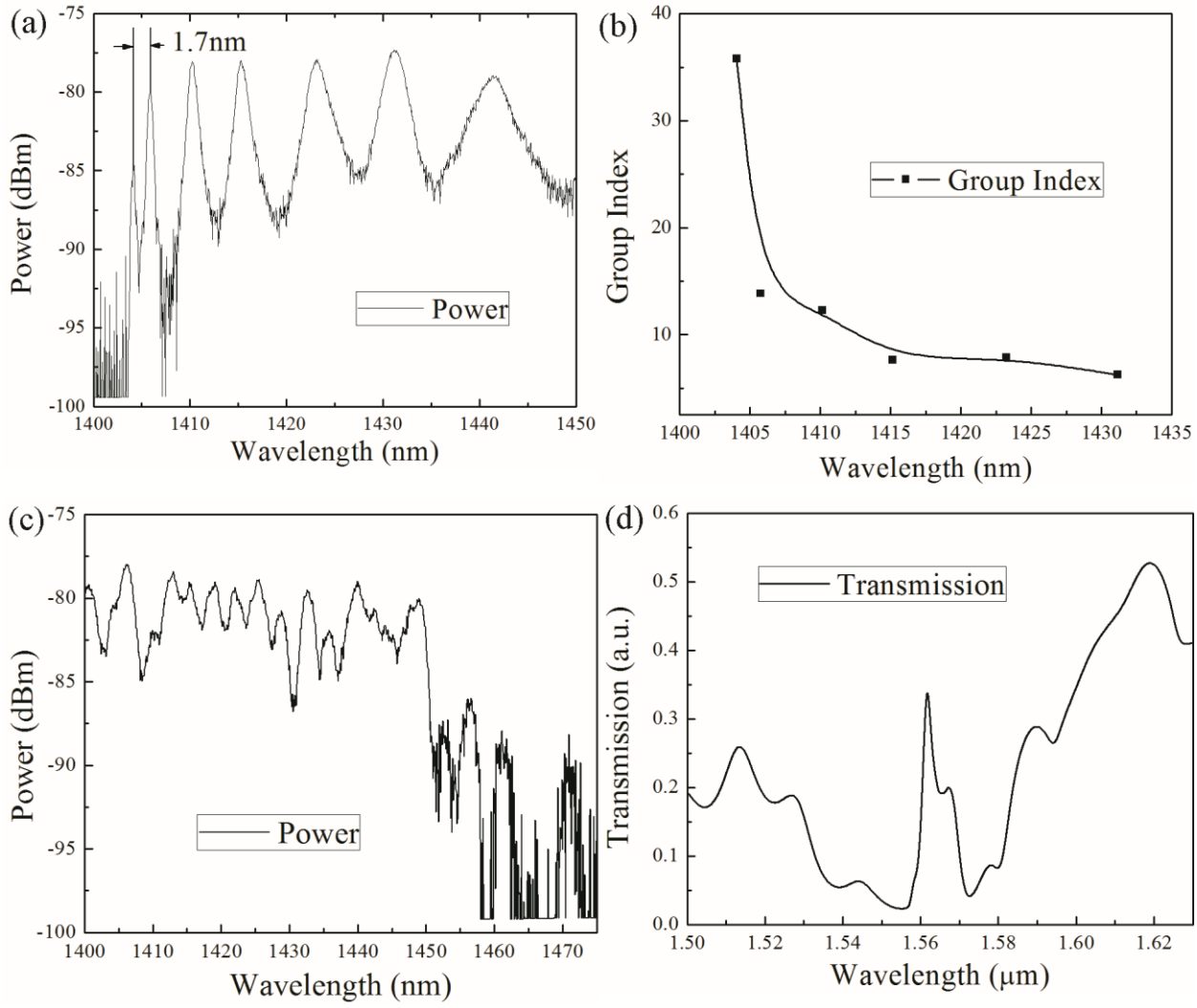

Fig. 34 (a) Measured transmission spectrum of rectangular hole nanobeam; (b) Group Index contour of rectangular hole integrated single armed slow light MZI; (c) Measured transmission spectrum of rectangular hole integrated single armed slow light MZI; (d) Simulated single armed MZI device with rectangular lattice holes

4.2 Bulk Sensing Experiments

For bulk sensing experiments, we applied salt water with different concentration, starting from 0.75% to 5.6%. From most diluted to most concentrated, the mass of salt are 0.0158g, 0.0335g, 0.0600g, 0.1010g and 0.1206g, respectively. They are resolved in 2g of water. Then each different type of solutions are injected into the inlet of microfluidic system to flow over devices. For every single step, the speed of injection is 0.005mL/min. We assure not to take measurement until the shift of spectrum is saturated after the devices are rinsed inside flow cell chamber for some time (10min – 15min). The refractive indices are measured using refractometer. The shift of each step versus the measured refractive index for two different structures plotted in Fig. 35. Note that all the data points are obtained from making Lorentzian fit to the band edge peak from original data.

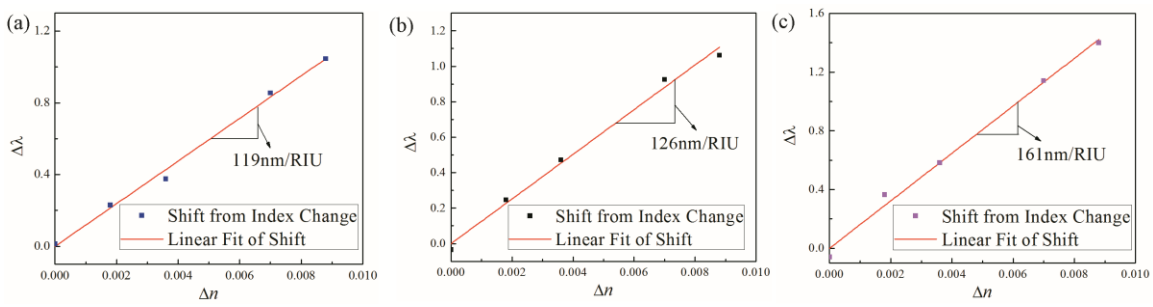

Fig. 35 (a) Bulk sensing shift and its linear fit of diamond hole nanobeam device; (b) Bulk sensing shift and its linear fit of diamond hole single armed MZI device; (c) Bulk sensing shift and its linear fit of rectangular hole nanobeam device.

For Fig. 35 (a), which represents the shift of diamond hole nanobeama device, the linear fit line has R2 value of 0.9862. The slope of this line is 119nm/RIU, which is lower than we expected. This is probably due to the relatively less light-matter overlap compared to simulated scenario. In comparison, by applying exactly the same experiment process and the shift versus index change curve for single armed MZI is plotted in Fig. 35 (b). We can see that the slope for

the fitted curve of single armed MZI device is larger, which is 126nm/RIU. This also verifies the mechanism we have discussed: higher group index will enable the device to have higher sensitivity when integrated in MZIs. By converting this value into typical type of MZI sensitivity, we have 170,000rad/RIU-cm and 180,000rad/RIU-cm for nanobeam and single arm MZI device, respectively. From Fig. 35 (c), we can observe a spectral sensitivity of 161nm/RIU for the. This is the result obtained from rectangular nanobeam devices. Even this is the highest sensitivity we observed from experiment, but this is due to the larger dimension of rectangular hole which leads to higher LMI. This also results in the operation wavelength ~100nm away from desire range. Thus we would not treat these results comparable to the other two cases.

4.3 Surface Sensing Experiments

The surface sensing recipe is originally cited from the previous recipe by J. Lawrie et al. [68,69] that our lab used and later modified by K. R. Beavers et al. [70]. The main steps are illustrated in Fig. 36. This process basically is to attach some specific sequence of DNA to the functionalized silicon surface. Then use the matched DNA to bind with DNA probe and test optical shift after each surface functionalization step.

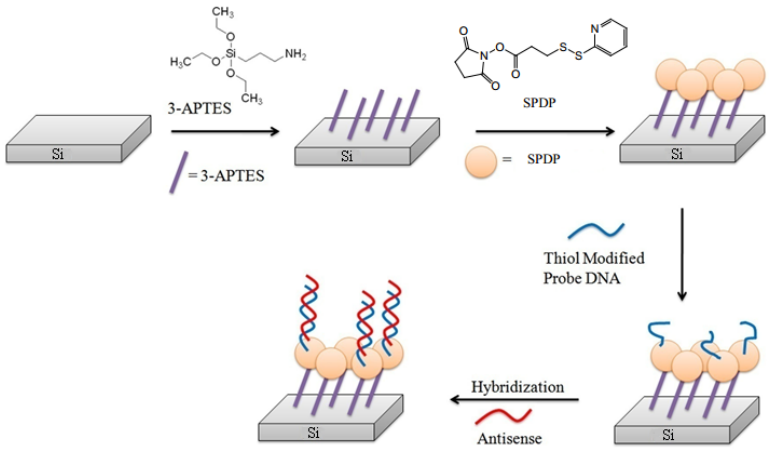

Fig. 36 Flowchart of pre-synthesized DNA binding experiment (Figure from Ref. [71])

To be specific, the first step is to passivate the surface of silicon device. This will make the surface of silicon exists a thin layer of oxide. This OH ending functional group will enable the bonding of silicon with the linker, which is (3-Aminopropyl) triethoxysilane (3-APTES) in this case. The passivation process is to place the sample in furnace for 10 minutes at 500℃ to grow the thermal oxide layer, and then soak the sample in 1% 3-APTES solution of toluene for 15 minutes. After that, another heating step is needed for annealing the 3-APTES. It is achieved with 20 minutes under 150℃.

Next, we are applying an amine-to-sulfhydryl heterobifunctional crosslinker, N-succinimidyl 3-(2-pyridyldithio) propionate (SPDP) dissolved in ethanol with the concentration of 2mg/mL. SPDP is a linker molecule to connect probe DNA and silane that has already attached to the surface of silicon. SPDP solution reacted with silanized silicon device for 30 minutes. This SPDP linking will be followed by soaking in IPA for 5 minutes then rinsing with IPA/Ethanol twice. Then probe DNA (5'-TAG CTA TGG TCC TCG T-3', 3' Thiol C3, Eurofins MWG Operon) should be reduced before attachment to SPDP crosslink. This was achieveld on TCEP resin. The concentration of probe DNA is 10μM and resolved in deionized water. Then we dropped the solution to the surface of our device. This step will take 1 hour. After probe binding to functionalized silicon surface, a 20 minutes soaking step in HEPES buffer is needed to remove non-specific bonded molecules.

Finally, the complementary target DNA (with the sequence of ACG AGG ACC ATA GCT A) is heated to 37℃ and dropped to the surface of probe attached silicon. DNA hybridization will take 1 hour. Then another round of HEPES buffer soaking will be necessary for eliminating non-hybridized oligos.

We assure that during each measurement, the device was under same circumstance (air). And the spectrum shifting spectra for both single armed MZI devices as well as nanobeam are demonstrated in Fig. 37.

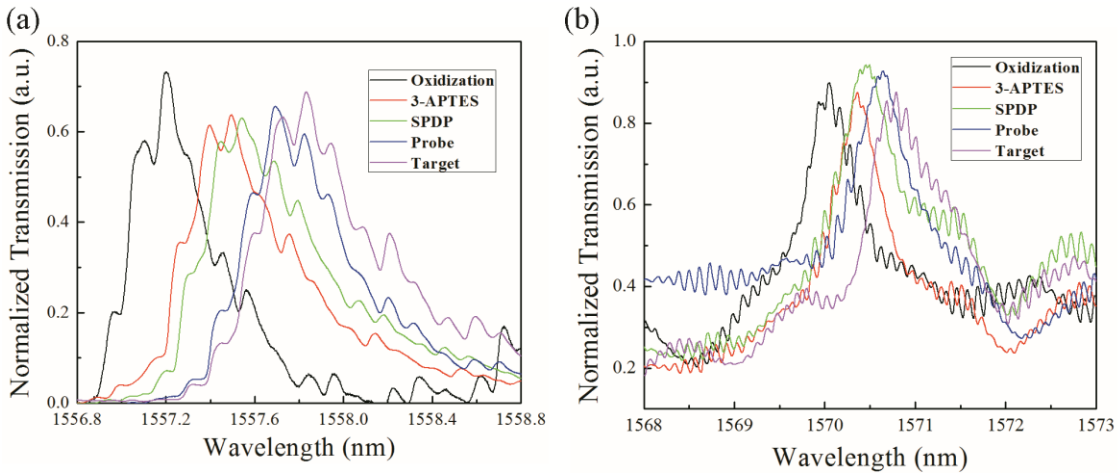

Fig. 37 (a) Spectrum shift of diamond hole nanobeam for pre-synthesized DNA binding experiment; (b) Spectrum shift of single armed MZI with diamond holes for DNA binding experiment. (Note: The wavelength axes have been modified to display the range that can demonstrate the entire peaks of spectra that are at the band edge wavelengths)

In order to better quantify the shifts, we listed a table below for comparison. See Table 3 for details.

Table 3 Surface sensing performance for diamond hole slow light devices

Surface Sensing Shift (nm)	Oxide	3-APTES	SPDP	Probe	Target
Diamond Hole Nanobeam	-1.394	0.293	0.05	0.151	0.137
Diamond Hole MZI Single	-0.961	0.316	0.134	0.147	0.144

From the data collected in Table 3, most are comparable. Only the 3-APTES step for single armed MZI is oddly larger than that of nanobeam. Whereas the SPDP shift for nanobeam

spectrum is less than usual. In order to reach a firm conclusion regarding these structures, more experiments need conducting to eliminate sample-to-sample variation. Nonetheless, the surface sensitivity of slow light MZI is comparable to those optical biosensors applying resonators, which will make it more stable and thermal fluctuation shield.

Chapter 5: Summary and Future Works

In summary, we reviewed the field of label-free optical biosensors with regards to device topology and the fabrication process. We also introduced the fundamentals of microfluidics and microfluidic fabrication techniques. After that, we designed, fabricated and tested a novel type of label-free optical biosensor by integrating slow light waveguide into a Mach-Zehnder Interferometer. This device achieved a phase sensitivity as high as 100,000 rad/RIU-cm according to simulation results and 170,000 rad/RIU-cm according to experimental data, which is much higher than reported MZI biosensors. Apart from typical slow light structures, we also investigated slow light MZI with defect holes in order to achieve even better phase sensitivity. During this part of investigation, the highest simulated sensitivity was 223,000 rad/RIU-cm for a rectangular hole slow light MZI with multiple-defect holes. Specific detection of 16mer DNA molecules with a concentration of 10μM was also demonstrated using the slow light MZI platform. A 0.151nm red shift was observed, which is comparable to current reports of optical biosensors based on photonic cavities. More rounds of the specific binding detection experiments are in need for exploring the LOD of this device.

In the near future, additional rounds of three-dimensional FDTD simulation should be conducted in order to better approach theoretical prediction. In order to implement more cases concerning this simulation study, another round of fabrication is required. During this fabrication, the dimension of the rectangular hole photonic crystal should be adjusted to match simulated models and the fabrication of defect hole integrated slow light MZIs should be attempted. Also, based on our current study, we suspect that a longer device will benefit the slow light effect and will contribute more to enhancing sensitivity of the slow light integrated MZI devices. Thus we

suggest the fabrication of different lengths of the photonic crystal region in order to compare and analyze the corresponding sensitivities. Furthermore, we recommend designing a taper to help couple the light from an unstructured waveguide into the slow light region. In this way, the transmission spectrum of single armed slow light MZIs will be more decipherable.

In addition to biosensing, this novel type of MZI can be used for optical modulation. Because the slow light effect enhances the localized electric field intensity, less energy is required for modulation. This lower energy consuming modulator is essential for the next-generation network. In order to apply this design to optical modulation, III-V element doping techniques requires study. Specifically, the study should begin with the simulation of the doped device for modulation, followed by a III-V doping process on fabricated devices. Finally, high-frequency experiment should be implemented for characterizing the device's high speed performance.

References

1. http://marketpublishers.com/report/medicine_pharmaceuticals_biotechnology/drugs_biotechnology/biosensors_a_global_market_overview.html.

2. J. D. Joannopoulos, S. G. Johnson, J. N. Winn, and R. D. Meade. *Photonic crystals: molding the flow of light*. (Princeton university press, 2011).

3. M. A. Cooper, "Optical biosensors in drug discovery," *Nature Reviews Drug Discovery* **1**, 515-528 (2002).

4. A. Densmore, D.-X. Xu, S. Janz, P. Waldron, T. Mischki, G. Lopinski, A. Delâge, J. Lapointe, P. Cheben, and B. Lamontagne, "Spiral-path high-sensitivity silicon photonic wire molecular sensor with temperature-independent response," *Optics Letters* **33**, 596-598 (2008).

5. R. Heideman, R. Kooyman, and J. Greve, "Performance of a highly sensitive optical waveguide Mach-Zehnder interferometer immunosensor," *Sensors and Actuators B: Chemical* **10**, 209-217 (1993).

6. K. Kim, and T. E. Murphy, "Porous silicon integrated Mach-Zehnder interferometer waveguide for biological and chemical sensing," *Optics Express* **21**, 19488-19497 (2013).

7. Q. Liu, X. Tu, K. W. Kim, J. S. Kee, Y. Shin, K. Han, Y.-J. Yoon, G.-Q. Lo, and M. K. Park, "Highly sensitive Mach–Zehnder interferometer biosensor based on silicon nitride slot waveguide," *Sensors and Actuators B: Chemical* **188**, 681-688 (2013).

8. F. Prieto, B. Sepulveda, A. Calle, A. Llobera, C. Domínguez, A. Abad, A. Montoya, and L. M. Lechuga, "An integrated optical interferometric nanodevice based on silicon technology for biosensor applications," *Nanotechnology* **14**, 907 (2003).

9. X. Tu, J. Song, T.-Y. Liow, M. K. Park, J. Q. Yiying, J. S. Kee, M. Yu, and G.-Q. Lo, "Thermal independent silicon-nitride slot waveguide biosensor with high sensitivity," *Optics Express* **20**, 2640-2648 (2012).

10. J. Wo, G. Wang, Y. Cui, Q. Sun, R. Liang, P. P. Shum, and D. Liu, "Refractive index sensor using microfiber-based Mach–Zehnder interferometer," *Optics Letters* **37**, 67-69 (2012).

11. H. Yu, L. Xiong, Z. Chen, Q. Li, X. Yi, Y. Ding, F. Wang, H. Lv, and Y. Ding, "Ultracompact and high sensitive refractive index sensor based on Mach–Zehnder interferometer," *Optics and Lasers in Engineering* **56**, 50-53 (2014).

12. B. J. Lee, S. G. Kim, and H. L. Sohn, "Optically encoded smart dust from DBR porous silicon," *Key Engineering Materials* **321**, 53-56 (2006).

13. N. C. Lindquist, A. Lesuffleur, H. Im, and S.-H. Oh, "Sub-micron resolution surface plasmon resonance imaging enabled by nanohole arrays with surrounding Bragg mirrors for enhanced sensitivity and isolation," *Lab on a Chip* **9**, 382-387 (2009).

14. G. A. Rodriguez, J. D. Ryckman, Y. Jiao, and S. M. Weiss, "A size selective porous silicon grating-coupled Bloch surface and sub-surface wave biosensor," *Biosensors and Bioelectronics* **53**, 486-493 (2014).

15. S. Chakravarty, Y. Zou, W.-C. Lai, and R. T. Chen, "Slow light engineering for high< i> Q</i> high sensitivity photonic crystal microcavity biosensors in silicon," *Biosensors and Bioelectronics* **38**, 170-176 (2012).

16. S. C. Buswell, V. A. Wright, J. M. Buriak, V. Van, and S. Evoy, "Specific detection of proteins using photonic crystal waveguides," *Optics express* **16**, 15949-15957 (2008).

17. B. Cunningham, P. Li, B. Lin, and J. Pepper, "Colorimetric resonant reflection as a direct biochemical assay technique," *Sensors and Actuators B: Chemical* **81**, 316-328 (2002).

18. Y. Guo, J. Y. Ye, C. Divin, B. Huang, T. P. Thomas, J. Baker, James R, and T. B. Norris, "Real-time biomolecular binding detection using a sensitive photonic crystal biosensor," *Analytical Chemistry* **82**, 5211-5218 (2010).

19. C. Kang, and S. M. Weiss, "Photonic crystal with multiple-hole defect for sensor applications," *Optics Express* **16**, 18188-18193 (2008).

20. M. R. Lee, and P. M. Fauchet, "Two-dimensional silicon photonic crystal based biosensing platform for protein detection," *Optics Express* **15**, 4530-4535 (2007).

21. M. G. Scullion, A. Di Falco, and T. F. Krauss, "Slotted photonic crystal cavities with integrated microfluidics for biosensing applications," *Biosensors and Bioelectronics* **27**, 101-105 (2011).

22. R. W. Boyd, and J. E. Heebner, "Sensitive disk resonator photonic biosensor," *Applied Optics* **40**, 5742-5747 (2001).

23. S. M. Grist, S. A. Schmidt, J. Flueckiger, V. Donzella, W. Shi, S. Talebi Fard, J. T. Kirk, D. M. Ratner, K. C. Cheung, and L. Chrostowski, "Silicon photonic micro-disk resonators for label-free biosensing," *Optics Express* **21**, 7994-8006 (2013).

24. F. Vollmer, and S. Arnold, "Whispering-gallery-mode biosensing: label-free detection down to single molecules," *Nature Methods* **5**, 591-596 (2008).

25. T. Claes, W. Bogaerts, and P. Bienstman, "Experimental characterization of a silicon photonic biosensor consisting of two cascaded ring resonators based on the Vernier-effect and introduction of a curve fitting method for an improved detection limit," *Optics Express* **18**, 22747-22761 (2010).

26. T. Claes, J. G. Molera, K. De Vos, E. Schachtb, R. Baets, and P. Bienstman, "Label-free biosensing with a slot-waveguide-based ring resonator in silicon on insulator," *Photonics Journal, IEEE* **1**, 197-204 (2009).

27. K. De Vos, J. Girones, T. Claes, Y. De Koninck, S. Popelka, E. Schacht, R. Baets, and P. Bienstman, "Multiplexed antibody detection with an array of silicon-on-insulator microring resonators," *Photonics Journal, IEEE* **1**, 225-235 (2009).

28. S. Hu, Y. Zhao, K. Qin, S. T. Retterer, I. I. Kravchenko, and S. M. Weiss. "In-Situ Synthesis of DNA Probe Molecules for Enhanced Sensitivity of Label-free Optical Biosensors," Manuscript submitted to *ACS Photonics* (2014).

29. M. Khorasaninejad, N. Clarke, M. P. Anantram, and S. S. Saini, "Optical bio-chemical sensors on SNOW ring resonators," *Optics Express* **19**, 17575-17584 (2011).

30. H. C. Nguyen, Y. Sakai, M. Shinkawa, N. Ishikura, and T. Baba, "10 Gb/s operation of photonic crystal silicon optical modulators," *Optics Express* **19**, 13000-13007 (2011).

31. S. Weiss, M. Molinari, and P. Fauchet, "Temperature stability for silicon-based photonic band-gap structures," *Applied Physics Letters* **83**, 1980-1982 (2003).

32. http://en.wikipedia.org/wiki/Mach%E2%80%93Zehnder_interferometer.

33. R. Aalipour, and M. Aminjafari, "Phase shift calibration based on Fresnel diffraction from phase plates," *Journal of Optics* **14**, 125706 (2012).

34. F. Xia, L. Sekaric, and Y. Vlasov, "Ultracompact optical buffers on a silicon chip," *Nature Photonics* **1**, 65-71 (2007).

35. K. Gondaira, K. Ishizaki, and S. Noda, "Influence of structural fluctuations on Q factor of nanocavities at the surface of three-dimensional photonic crystals," *JOSA B* **30**, 1660-1664 (2013).

36. K. Ishizaki, K. Gondaira, Y. Ota, K. Suzuki, and S. Noda, "Nanocavities at the surface of three-dimensional photonic crystals," *Optics Express* **21**, 10590-10596 (2013).

37. K. Ishizaki, M. Koumura, K. Suzuki, K. Gondaira, and S. Noda, "Realization of three-dimensional guiding of photons in photonic crystals," *Nature Photonics* **7**, 133-137 (2013).

38. S. Noda, M. Yokoyama, M. Imada, A. Chutinan, and M. Mochizuki, "Polarization mode control of two-dimensional photonic crystal laser by unit cell structure design," *Science* **293**, 1123-1125 (2001).

39. A. Brimont, D. Thomson, P. Sanchis, J. Herrera, F. Gardes, J. Fedeli, G. Reed, and J. Mart ĺ "High speed silicon electro-optical modulators enhanced via slow light propagation," *Optics Express* **19**, 20876-20885 (2011).

40. Q. Quan, P. B. Deotare, and M. Loncar, "Photonic crystal nanobeam cavity strongly coupled to the feeding waveguide," *Applied Physics Letters* **96**, 203102 (2010).

41. Q. Quan, and M. Loncar, "Deterministic design of wavelength scale, ultra-high Q photonic crystal nanobeam cavities," *Optics Express* **19**, 18529-18542 (2011).

42. http://ab-initio.mit.edu/wiki/index.php/Main_Page.

43. J. D. Joannopoulos, P. R. Villeneuve, and S. Fan, "Photonic crystals: putting a new twist on light," *Nature* **386**, 143-149 (1997).

44. Q. Quan, I. B. Burgess, S. K. Tang, D. L. Floyd, and M. Loncar, "High-Q, low index-contrast polymeric photonic crystal nanobeam cavities," *Optics express* **19**, 22191-22197 (2011).

45. V. R. Almeida, Q. Xu, C. A. Barrios, and M. Lipson, "Guiding and confining light in void nanostructure," *Optics Letters* **29**, 1209-1211 (2004).

46. C. Kang, C. T. Phare, Y. A. Vlasov, S. Assefa, and S. M. Weiss, "Photonic crystal slab sensor with enhanced surface area," *Optics Express* **18**, 27930-27937 (2010).

47. http://groups.csail.mit.edu/cag/biostream/.

48. J. L. Arlett, E. B. Myers, and M. L. Roukes, "Comparative advantages of mechanical biosensors," *Nature Nanotechnology* **6**, 203-215 (2011).

49. K. Choi, J.-Y. Kim, J.-H. Ahn, J.-M. Choi, M. Im, and Y.-K. Choi, "Integration of field effect transistor-based biosensors with a digital microfluidic device for a lab-on-a-chip application," *Lab on a Chip* **12**, 1533-1539 (2012).

50. S. Choi, M. Goryll, L. Y. M. Sin, P. K. Wong, and J. Chae, "Microfluidic-based biosensors toward point-of-care detection of nucleic acids and proteins," *Microfluidics and Nanofluidics* **10**, 231-247 (2011).

51. V. N. Goral, N. V. Zaytseva, and A. J. Baeumner, "Electrochemical microfluidic biosensor for the detection of nucleic acid sequences," *Lab on a Chip* **6**, 414-421 (2006).

52. H. Im, X.-J. Huang, B. Gu, and Y.-K. Choi, "A dielectric-modulated field-effect transistor for biosensing," *Nature Nanotechnology* **2**, 430-434 (2007).

53. A. V. Kabashin, P. Evans, S. Pastkovsky, W. Hendren, G. A. Wurtz, R. Atkinson, R. Pollard, V. A. Podolskiy, and A. V. Zayats, "Plasmonic nanorod metamaterials for biosensing," *Nature Materials* **8**, 867-871 (2009).

54. H. Lee, E. Sun, D. Ham, and R. Weissleder, "Chip–NMR biosensor for detection and molecular analysis of cells," *Nature Medicine* **14**, 869-874 (2008).

55. X. Wei, J. W. Mares, Y. Gao, D. Li, and S. M. Weiss, "Biomolecule kinetics measurements in flow cell integrated porous silicon waveguides," *Biomedical Optics Express* **3**, 1993-2003 (2012).

56. F. K. Balagaddé, L. You, C. L. Hansen, F. H. Arnold, and S. R. Quake, "Long-term monitoring of bacteria undergoing programmed population control in a microchemostat," *Science* **309**, 137-140 (2005).

57. J. Lee, A. Sharei, W. Y. Sim, A. Adamo, R. Langer, K. F. Jensen, and M. G. Bawendi, "Nonendocytic delivery of functional engineered nanoparticles into the cytoplasm of live cells using a novel, high-throughput microfluidic device," *Nano Letters* **12**, 6322-6327 (2012).

58. S. Lin, E. Schonbrun, and K. Crozier, "Optical manipulation with planar silicon microring resonators," *Nano Letters* **10**, 2408-2411 (2010).

59. M. M. Wang, E. Tu, D. E. Raymond, J. M. Yang, H. Zhang, N. Hagen, B. Dees, E. M. Mercer, A. H. Forster, and I. Kariv, "Microfluidic sorting of mammalian cells by optical force switching," *Nature Biotechnology* **23**, 83-87 (2004).

60. M. Li, S. Li, J. Wu, W. Wen, W. Li, and G. Alici, "A simple and cost-effective method for fabrication of integrated electronic-microfluidic devices using a laser-patterned PDMS layer," *Microfluidics and Nanofluidics* **12**, 751-760 (2012).

61. H. Wu, T. W. Odom, D. T. Chiu, and G. M. Whitesides, "Fabrication of complex three-dimensional microchannel systems in PDMS," *Journal of the American Chemical Society* **125**, 554-559 (2003).

62. E. Yablonovitch, and T. Gmitter, "Photonic band structure: The face-centered-cubic case," *Physical Review Letters* **63**, 1950 (1989).

63. C. Kang. "Multi-Hole Defects: Optimizing Light-Matter Interaction in Photonic Crystal Cavities," Doctoral Dissertation, Vanderbilt University, (2011).

64. S. Hu, K. Qin, I. I. Kravchenko, S. T. Retterer and S. M. Weiss, "Suspended Micro-Ring Resonator for Enhanced Biomolecule Detection Sensitivity," *in Proceedings of SPIE* **8933**, 89330606 (2014).

65. J. D. Ryckman, and S. M. Weiss, "Localized field enhancements in guided and defect modes of a periodic slot waveguide," *Photonics Journal, IEEE* **3**, 986-995 (2011).

66. http://www.elveflow.com/microfluidic-reviews-and-tutorials/microfluidics-and-microfluidic-devices-a-review.

67. T. J. Levario, M. Zhan, B. Lim, S. Y. Shvartsman, and H. Lu, "Microfluidic trap array for massively parallel imaging of Drosophila embryos," *Nature Protocols* **8**, 721-736 (2013).

68. J. L. Lawrie, Y. Jiao, and S. M. Weiss, "Size-dependent infiltration and optical detection of nucleic acids in nanoscale pores," *Nanotechnology, IEEE Transactions on* **9**, 596-602 (2010).

69. X. Wei , C. Kang , G. Rong , S. T. Retterer and S. M. Weiss, "Porous silicon waveguide with integrated grating coupler for DNA sensing," *in Proceedings of SPIE* **7167**, 71670C (2009).

70. K. R. Beavers, J. W. Mares, C. M. Swartz, Y. Zhao, S. M. Weiss, and C. L. Duvall. "In Situ Synthesis of Peptide Nucleic Acids in Porous Silicon for Drug Delivery and Biosensing," Manuscript submitted to *Bioconjugate Chemistry* (2014).

71. X. Wei. "Porous Silicon Waveguide Biosensors with a Grating Coupler," Doctoral Dissertation, Vanderbilt University, (2012).